Short article

Cell Metabolism

Ergothioneine improves healthspan of aged animals by enhancing cGPDH activity through CSE-dependent persulfidation

Graphical abstract

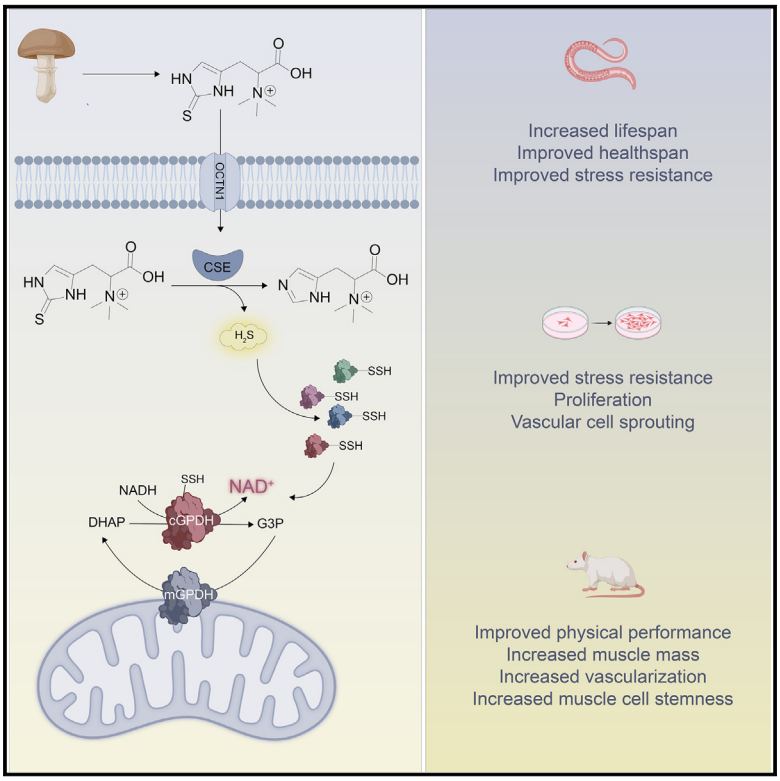

Authors

Dunja Petrovic, Luke Slade, Yiorgos Paikopoulos, ..., Michael P. Murphy, Vesna Otasevic, Milos R. Filipovic

Correspondence

milos.filipovic@glasgow.ac.uk

In brief

Petrovic et al. demonstrate that ergothioneine acts as an alternative substrate for cystathionine gamma-lyase, an H_2S-producing enzyme, leading to an increase of protein persulfidation. The persulfidation of cGPDH enhances its activity, resulting in a boost of NAD^+ levels. Treatment with ergothioneine improves healthspan and physical performance in aged animals.

Highlights

- Ergothioneine enhances lifespan and healthspan in aged *C. elegans* and rats
- These effects are dependent on CSE-catalyzed H_2S production and persulfidation
- Ergothioneine boosts NAD^+ levels
- Ergothioneine-induced persulfidation of cGPDH enhances its NAD^+ formation

Petrovic et al., 2025, Cell Metabolism *37*, 542–556
February 4, 2025
https://doi.org/10.1016/j.cmet.2024.12.008

CellPress

CellPress
OPEN ACCESS

Cell Metabolism

Short article

Ergothioneine improves healthspan of aged animals by enhancing cGPDH activity through CSE-dependent persulfidation

Dunja Petrovic,[1] Luke Slade,[1,15] Yiorgos Paikopoulos,[1,15] Davide D'Andrea,[1,15] Nevena Savic,[2] Ana Stancic,[2] Jan Lj Miljkovic,[3] Thibaut Vignane,[1] Maria Kyriaki Drekolia,[4] Dusan Mladenovic,[5] Nikola Sutulovic,[6] Alice Refeyton,[7] Milica Kolakovic,[8] Vladimir M. Jovanovic,[9] Jasmina Zivanovic,[2] Marko Miler,[2] Valentina Vellecco,[10] Vincenzo Brancaleone,[11] Mariarosaria Bucci,[10] Alva M. Casey,[3] ChakShun Yu,[3] Siva Swapna Kasarla,[1] Karl William Smith,[1] Ayten Kalfe-Yildiz,[1] Martin Stenzel,[1] Antonio Miranda-Vizuete,[12] Roland Hergenröder,[1] Prasad Phapale,[1] Olivera Stanojlovic,[6] Ivana Ivanovic-Burmazovic,[8] Marija Vlaski-Lafarge,[7] Sofia-Iris Bibli,[4] Michael P. Murphy,[3,13] Vesna Otasevic,[2] and Milos R. Filipovic[1,14,16,*]

[1]Leibniz Institute for Analytical Sciences, ISAS e.V., Dortmund, Germany
[2]Institute for Biological Research "Sinisa Stankovic", National Institute of the Republic of Serbia, University of Belgrade, Belgrade, Serbia
[3]MRC Mitochondrial Biology Unit, University of Cambridge, Keith Peters Building, Cambridge CB2 0XY, UK
[4]Department of Vascular Dysfunction, European Center for Angioscience, Medical Faculty Mannheim, Heidelberg University, Mannheim, Germany
[5]Institute for Pathophysiology "Ljubodrag Buba Mihailovic", Faculty of Medicine, University of Belgrade, Belgrade, Serbia
[6]Laboratory for Neurophysiology, Institute for Medical Physiology "Richard Burian", Faculty of Medicine, University of Belgrade, Belgrade, Serbia
[7]Inserm U1211 Maladies Rares: Génétique et Métabolisme, Université de Bordeaux, Bordeaux, France
[8]Department of Chemistry, Ludwig Maximilians University of Munich, Munich, Germany
[9]Bioinformatics Solution Center, Institute for Informatics, Freie Universität Berlin, Berlin, Germany
[10]Department of Pharmacy, School of Medicine and Surgery, University of Naples Federico II, Naples, Italy
[11]Department of Science, University of Basilicata, Potenza, Italy
[12]Redox Homeostasis Group, Instituto de Biomedicina de Sevilla (IBIS), Hospital Universitario Virgen del Rocío/CSIC/Universidad de Sevilla, Seville, Spain
[13]Department of Medicine, University of Cambridge, Cambridge CB2 0QQ, UK
[14]School of Molecular Biosciences, College of Medical Veterinary and Life Sciences, University of Glasgow, Glasgow, UK
[15]These authors contributed equally
[16]Lead contact
*Correspondence: milos.filipovic@glasgow.ac.uk
https://doi.org/10.1016/j.cmet.2024.12.008

SUMMARY

Ergothioneine (ET), a dietary thione/thiol, is receiving growing attention for its possible benefits in healthy aging and metabolic resilience. Our study investigates ET's effects on healthspan in aged animals, revealing lifespan extension and enhanced mobility in *Caenorhabditis elegans*, accompanied by improved stress resistance and reduced age-associated biomarkers. In aged rats, ET administration enhances exercise endurance, muscle mass, and vascularization, concomitant with higher NAD^+ levels in muscle. Mechanistically, ET acts as an alternative substrate for cystathionine gamma-lyase (CSE), stimulating H_2S production, which increases protein persulfidation of more than 300 protein targets. Among these, protein-persulfidation-driven activation of cytosolic glycerol-3-phosphate dehydrogenase (cGPDH) primarily contributes to the ET-induced NAD^+ increase. ET's effects are abolished in models lacking CSE or cGPDH, highlighting the essential role of H_2S signaling and protein persulfidation. These findings elucidate ET's multifaceted actions and provide insights into its therapeutic potential for combating age-related muscle decline and metabolic perturbations.

INTRODUCTION

The aging process is inevitably accompanied by a decline in healthspan and physiological function, posing considerable challenges to healthcare systems worldwide. Seeking solutions to mitigate age-related deterioration and enhance overall well-being has become a pressing endeavor in recent years. One intriguing avenue of exploration involves the investigation of natural compounds with potential therapeutic properties.[1–4] Among these, ergothioneine (ET) (Figure 1A), a naturally occurring thiol

CellPress
OPEN ACCESS

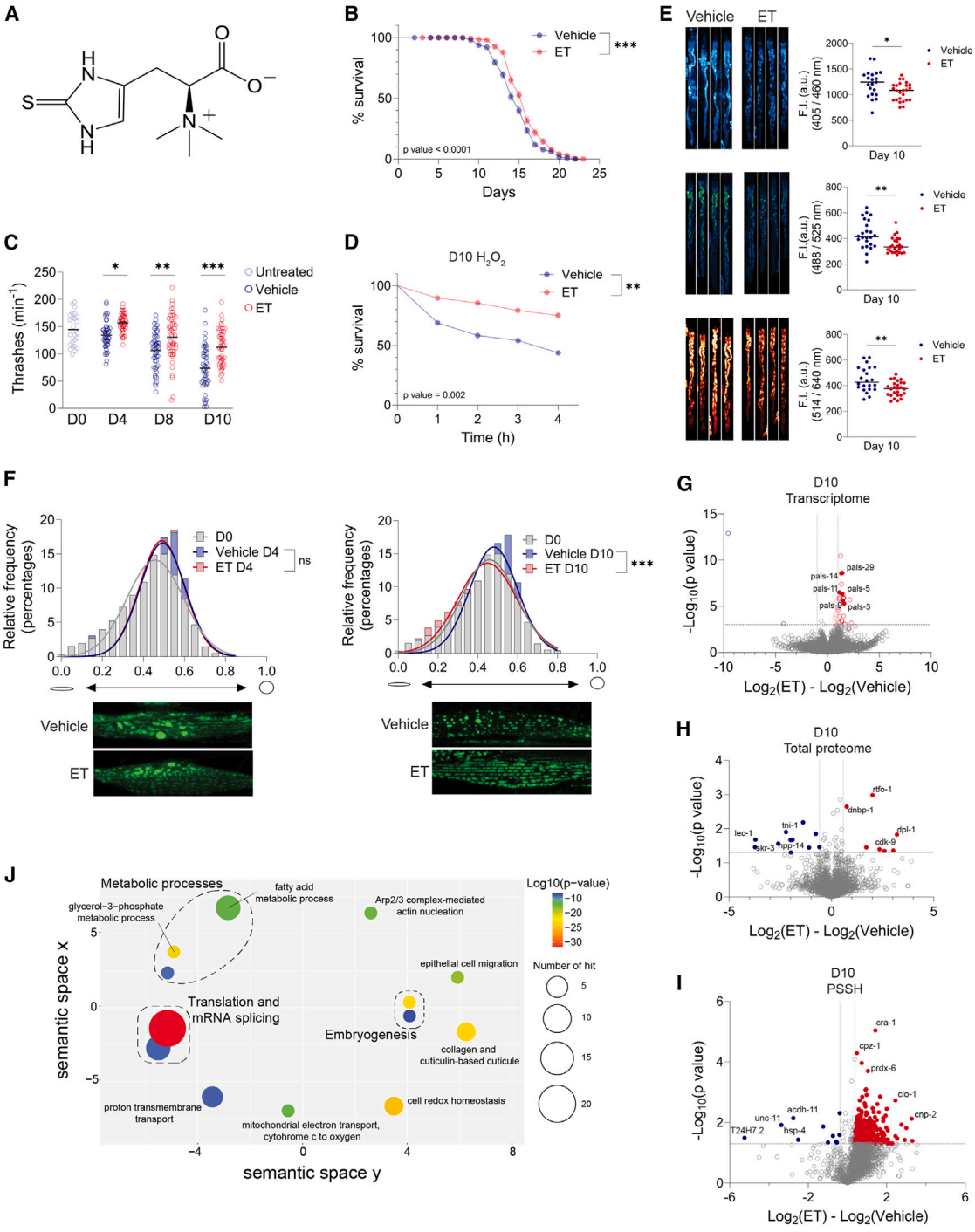

Figure 1. ET improves lifespan and healthspan of *C. elegans*

(A) Chemical structure of ergothioneine (ET).

(B) Lifespan of ET (450 μM)-treated wild-type (N2) worms (6.8% ± 0.3% for median and 22 vs. 23 days for the maximal lifespan; $N \geq 460$ animals per group, Kaplan-Meier survival analysis and Mantel-Cox long rank test).

(C) Movement capacity (the number of thrashing movements made by each worm in 60 s) of aged worms treated with 450 μM ET ($N = 50$ per experimental group, two-way ANOVA, $^{*}p < 0.05$, $^{**}p < 0.01$, $^{***}p < 0.001$).

(D) Survival curves of ET (450 μM)-treated D10 worms exposed to 100 μM H_2O_2 ($N = 48$ per experimental group; Mantel-Cox long rank test, $^{**}p < 0.01$).

(E) Blue, green, and red autofluorescence of D10 worms treated with 450 μM ET ($N > 20$, unpaired Student's t test, $^{*}p < 0.05$, $^{**}p < 0.01$).

(F) Mitochondrial morphology of worms treated with 450 μM ET. Confocal images and quantification of mitochondrial roundness in green fluorescent protein (GFP)-labeled mitochondria in young adults (D0) and aged (D4 and D10) Pmyo-3::mitoGFP worms ($N > 20$ worms, one or more muscle cells per worm, one-way ANOVA, $^{***}p < 0.001$).

(legend continued on next page)

compound found in dietary sources such as fungi and Actinomycetes,[5] has emerged as a promising candidate for promoting healthy aging and improving metabolic resilience.[6–9]

ET accumulates in cells in high amounts via the OCTN1 (Slc22a4) transporter,[10] which is present not only in mammals but also in *C. elegans* (analog of the gene is *oct-1*).[11] Although it was initially suggested that ET exerts beneficial effects through antioxidant action,[6,12] its reduction potential (Em ∼−60 mV) is less reducing than many other antioxidants, and, therefore, ET is unreactive toward most oxidants produced in cells, such as hydrogen peroxide.[6,13] Recent studies suggested that administration of ET promotes longevity and healthy aging in male mice.[14] Blood ET levels inversely correlate with aging and several aging-related diseases, such as Parkinson's and Alzheimer's diseases, irrespective of dietary source.[9,15] Furthermore, administration of ET has shown protective effects against β-amyloid-induced neuronal injury and cytotoxicity, and demonstrates improvements in ischemia-reperfusion injury.[8]

In this study, our objective was to explore the potential impact of ET supplementation on the healthspan of aged animals and to elucidate the underlying mechanisms driving such effects. Our findings reveal that ET serves as an alternative substrate for cystathionine gamma-lyase (CSE), a pro-longevity gene,[16] leading to enhanced hydrogen sulfide (H_2S) production and subsequent protein persulfidation (PSSH). ET treatment resulted in increased mitochondrial respiration, ATP production, and cell growth, accompanied by elevated NAD^+ levels, both *in vitro* and *in vivo*. These changes occurred through persulfidation and activation of cytosolic glycerol-3-phosphate dehydrogenase (cGPDH), which increased NAD^+ levels to improve muscle mass, vascularization, muscle cell stemness, and treadmill endurance in aged rats. By unraveling the molecular intricacies of ET's actions, our research provides a foundation for further investigation into its clinical applications and therapeutic implications.

RESULTS

We started by testing the effect of ET on the lifespan of *C. elegans*. Treatment with 5 mM ET from day 1 adulthood (D1) resulted in significant median lifespan extension (20% ± 2%, Figure S1A; Table S1). Even when reducing the concentration to 450 μM we could still observe small but significant extensions in both median and maximal lifespans (Figure 1B; Table S1). More importantly, we noticed that mobility (thus healthspan) of ET-treated worms was markedly improved (Figure S1B; Video S1). *C. elegans* display age-related decline in thrashing performance,[17] and 450 μM ET maintained those rates quite high, even in day-10 adults (D10) (Figure 1C). We, therefore, focused on ET's effects on healthspan parameters during aging.

ET treatment increased resistance of D10 adults to H_2O_2, paraquat, arsenite, and heat stress (Figures 1D and S1C–S1E), suggesting global healthspan benefits even in old animals. The age-related increase in intestinal autofluorescence (sometimes referred to as lipofuscin or "age pigment"), measured via blue, green, and red wavelength autofluorescence,[18] was significantly lower in ET-treated animals (Figure 1E). Lipid accumulation, assessed by Oil Red and Nile Red fluorescence, was also significantly lower in ET-treated D10 adults (Figures S1F and S1G). Interestingly ET treatment did not affect the levels of 4-hydroxynonenal-modified proteins (Figure S1H), suggesting that ET has no effect on age-related lipid peroxidation.

It is important to note that the observed effects are not caused by OP50 bacteria used to feed *C. elegans*. Namely, ET effects on median and maximal lifespan (Figure S1I; Table S1) and on healthspan (Figures S1I–S1K) were still retained when animals were grown on UV-killed bacteria.

Structural deterioration of mitochondria represents a key aging hallmark in *C. elegans*.[19] We compared the mitochondrial network in SJ4103 [Pmyo-3::mitoGFP] animals expressing GFP in body-wall mitochondria to observe that ET treatment results in fewer fragments and more elongated mitochondria when compared with untreated aged animals (Figure 1F), which would explain the strong effect that ET has on motility.

To understand the lifespan/healthspan-preserving mechanisms of ET, we performed global proteome and transcriptome analyses of D4 and D10 adult worms. Aging is known to induce strong proteome and transcriptome remodeling in *C. elegans*,[20,21] so it came as a surprise that a very small number of targets were found to be significantly changing (±1.5-fold change for proteomics and ±2-fold change for transcriptomic analysis) in response to ET treatment, with no overlap between transcriptomic-proteomic datasets (Figures 1G, 1H, and S2A–S2C; Tables S2, S3, S4, and S5). Although no particular gene ontology (GO) term pathway enrichment could be observed, transcriptionally upregulated genes encompassed a family of proteins containing ALS2cr12 signatures (*pals-1*, *pals-3*, *pals-16*, etc.) known to be affected in *daf-16* mutants as well as by the treatments of different organosulfur compounds. Therefore, we tested the possibility that *daf-16* might be responsible for the beneficial effects of ET. The *daf-16* mutants exhibited the same lifespan extension observed in wild-type N2 animals (Figure S2D; Table S1), suggesting that *daf-16* expression is dispensable for ET's beneficial effects. Together, these data strongly suggest that the ET's effects are not caused by the transcriptional and translational regulation but most probably by the posttranslational modifications of the proteins.

ET is an organosulfur compound, a derivative of thiourea (Figure 1A), and thiourea derivatives are known to decompose to H_2S or elemental sulfur.[22,23] As H_2S is an emerging regulator of cellular function that acts through a posttranslational modification of proteins called PSSH,[24,25] we tested the hypothesis that the beneficial effects of ET might come from changes in PSSH. PSSH levels are reported to decrease in aging animals and their restoration via sulfide donors improves the resistance of animals

(G) Volcano plot of RNA-seq data showing differentially regulated genes (upregulated genes in red, downregulated genes in blue) in D10 animals treated with 450 μM ET.
(H) Volcano plot analysis of total proteome changes (upregulated proteins in red, downregulated proteins in blue) in D10 animals treated with 450 μM ET.
(I) Volcano plot analysis of persulfidome changes in D10 animals treated with 450 μM ET.
(J) GO term enrichment (biological process) of the 368 proteins exhibiting significantly higher persulfidation levels in ET treatment. Enrichment was performed using DAVID and the results visualized through REVIGO (p value ≤ 0.01).

CellPress
OPEN ACCESS

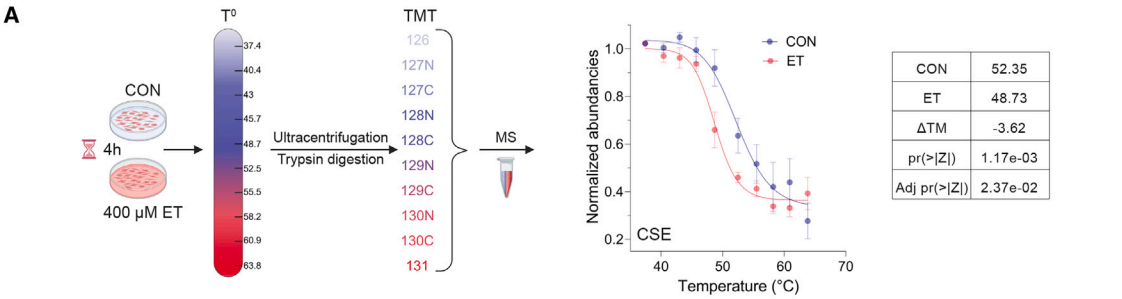

CON	52.35
ET	48.73
ΔTM	-3.62
pr(>|Z|)	1.17e-03
Adj pr(>|Z|)	2.37e-02

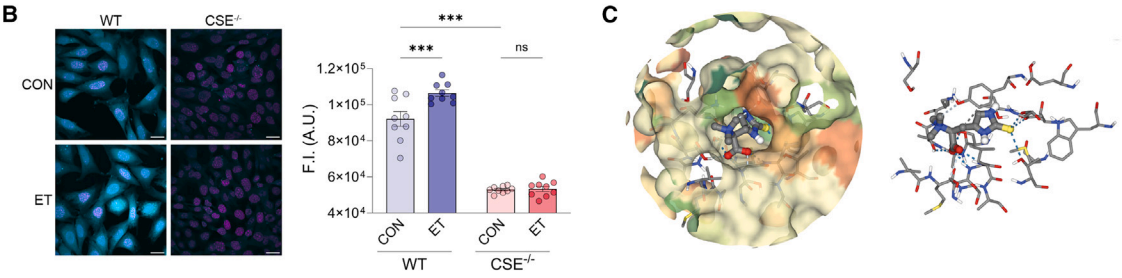

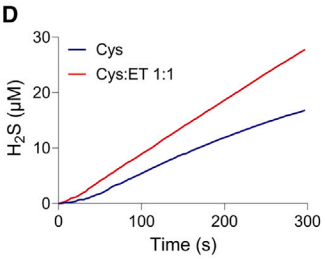

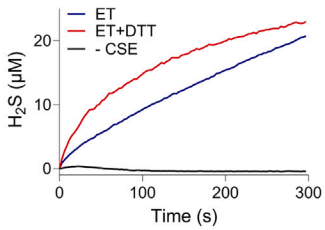

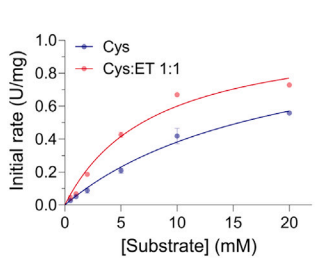

	V_{max} (U/mg)	K_m (mM)	k_{cat} (s^{-1})	k_{cat}/K_m ($mM^{-1}s^{-1}$)
Cys	1.06	17	0.79	0.046
ET	1.02	6.6	0.77	0.117

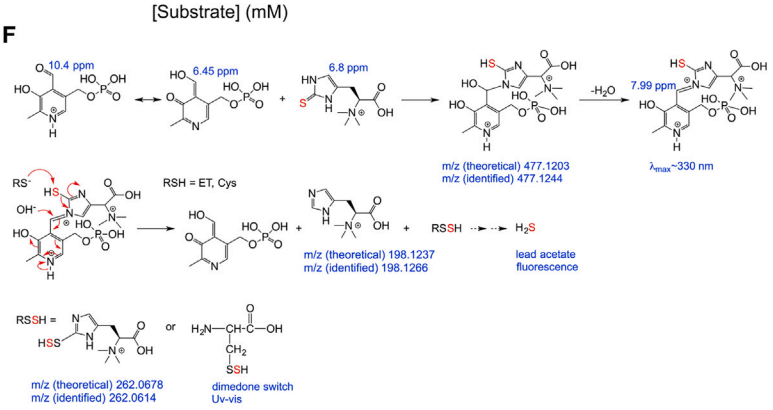

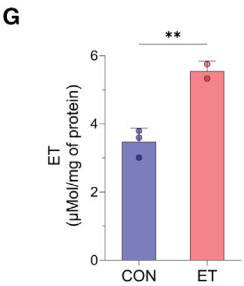

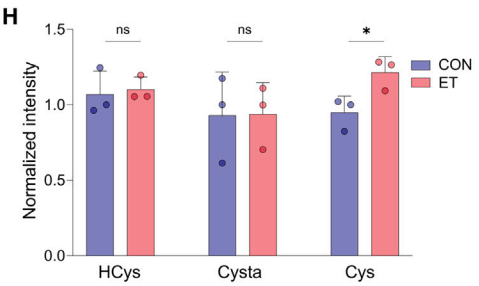

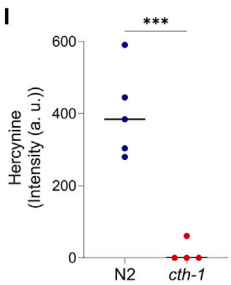

(legend on next page)

to oxidative stress.[26] We applied the dimedone-switch method for persulfidomic analysis and compared PSSH levels in untreated and ET-treated D10 worms. Unlike in the case of global proteome and transcriptome, we found that PSSH levels of >300 out of 2,737 endogenously persulfidated proteins significantly increased in ET-treated worms (Figure 1I; Table S6). The one-sided volcano plot indicates a strong unidirectional effect toward an increase in protein persulfidation. Normalization to protein expression levels found in the total proteome did not have major effects on the observed changes (Figure S2E). Identified protein targets are particularly enriched within the cytoplasmic vesicle lumen and mitochondrial ATP-synthase complex and have antioxidant activity, as well as copper-, NAD-, and FAD-binding activity, among others (Figures S2G and S2H). These proteins play a role in the mitochondrial electron transport process, cellular redox homeostasis, and embryogenesis, as well as in translation and metabolic processes such as fatty acid and glycerol-3-phosphate (G3P) metabolism (Figure 1J).

How does ET affect protein persulfidation? Although thiourea derivatives do decompose to produce H_2S,[22] this effect has not been observed in ET, which is quite stable under a physiological range of pHs and temperatures.[6,13] Using lysates of mouse embryonic fibroblasts (MEFs) treated with ET in the presence or absence of SDS (2%), we could observe that the ET-induced increase of PSSH is catalyzed by an enzyme (Figure S3A).

We used thermal proteome profiling[27,28] to identify potential binding targets for ET in MEFs (Figure 2A). A small number of proteins responded to ET treatment with significant thermal shift (Table S7). Among them, CSE was the only target that could potentially explain the PSSH effects (Figure 2A). Indeed, isothermal dose-response experiments confirmed the interaction of ET with CSE (Figure S3B). Of note, ET treatment of MEF cells does not affect the CSE expression levels (Data S1).

CSE is one of the three main H_2S-producing enzymes.[24] Treatment of MEFs with ET resulted in an increase of intracellular H_2S levels (Figure 2B). As expected, CSE knockout cells showed significantly impaired H_2S production, and the addition of ET did not change H_2S levels (Figure 2B), confirming that ET-induced H_2S production is controlled by CSE. To understand where in the CSE structure ET could bind, we performed *in silico* prediction of CSE-ET interaction using SeamDock.[29] We found that ET binds in the enzyme's active site pocket with binding affinity similar to that for its most-preferred substrate, cystathionine (5.8 kcal/mol for ET vs. 5.5 kcal/mol for cystathionine; Figure 2C). Two ligands showed strong overlay (Figure S3C and S3D), which suggested that ET could serve as an alternative substrate for CSE.

We assessed the ability of human recombinant CSE to consume ET and generate H_2S by incubating CSE with ET alone or in conjunction with cysteine (Figure 2D). H_2S production was faster and greater when ET was present, and ET alone produced H_2S, confirming that (1) ET is an alternative substrate for CSE and (2) it does not inhibit H_2S production from cysteine. Using a competitive two-substrate equation to estimate the kinetic parameters for CSE-catalyzed H_2S formation from ET, we could estimate V_{max} and K_m for the reaction (Figure 2E). While V_{max} did not differ between ET and cysteine, the K_m was significantly lower than what has been observed for cysteine. It is worth noting that the observed K_m for cysteine probably represents the mix of two K_m: one for the reaction in which H_2S and pyruvate are produced and the other one resulting in formation of H_2S and lanthionine.[30]

Although ET does not readily react with electrophilic thiol-blocking reagents,[31] we found that it can react with 4-chloro-7-nitrobenzofurazan to give an adduct with absorption maximum at ~400 nm. We used this feature to design an assay that allowed us to monitor the fate of ET's thione/thiol group in reaction with CSE. Indeed, we observed that CSE catalyzes "desulfuration" of ET (Figure S3E) to give hercynine, which was confirmed by mass spectrometry (MS) (Figures S3F and S3G).

Mechanistically, this reaction has to be catalyzed by pyridoxal phosphate (PLP) (Figure 2F), which is a main cofactor in CSE-catalyzed reactions.[24] Incubation of PLP with ET resulted in ultraviolet-visible (UV-vis) spectral shift from ~390 to ~330 nm (Figure S3H), characteristic for a Schiff base formation observed in other PLP reactions.[32] MS analysis of the reaction mixture

Figure 2. Ergothioneine is a substrate for CSE to produce H_2S

(A) Schematic representation of thermal proteome profiling of live, ET-treated MEFs (left) and observed melting curves for CSE (right). MEF cells were treated with 400 μM ET for 4 h. $n = 3$.

(B) SF7-AM fluorescence-probe-based detection of H_2S production in wild-type and $CSE^{-/-}$ MEF cells treated with 200 μM ET for 4 h. 3–5 images were analyzed per biological replicate ($n = 3$). Two-way ANOVA, $^{***}p < 0.001$.

(C) Docking results from SeamDock are shown for ET and human CSE (PDB: 2NMP). Left: the zoom at the protein active site with the ball-and-stick model of ET (carbon atoms are colored gray, nitrogen atoms blue, oxygen atoms red, and sulfur atoms yellow) fitting in it. Protein surface is colored based on hydrophobicity, with the most hydrophilic being brown-red and the most hydrophobic green. Right: interaction of ET with amino acid residues of the CSE active site. The hydrogen bonds are shown in dotted lines.

(D) H_2S generation from 10 mM cysteine or the mixture of 10 mM cysteine and 10 mM ET (upper figure) catalyzed by the human recombinant CSE (9 μg). H_2S generation from the reaction mixture containing CSE (9 μg) and 10 mM ET (with or without addition of 1 mM DTT) is shown in the lower figure. Negative control containing only ET, without the enzyme (−CSE), is presented in black. The reaction of H_2S with lead acetate to form lead sulfide was monitored by the increase in absorbance at 390 nm in 50 mM HEPES buffer pH 7.4 and at 37°C.

(E) Kinetic analysis of the reaction of cysteine (blue line) or cysteine: ET equimolar mixture (red line) with human recombinant CSE (9 μg). A competitive two-substrate equation was used to estimate the kinetic parameters for CSE-catalyzed H_2S formation from ET.

(F) Proposed reaction mechanism for the pyridoxal phosphate (PLP)-catalyzed H_2S release from ET based on NMR, ESI-MS, and UV-vis measurements shown in Figure S3. ^{1}H NMR chemical shifts for the key protons identified are marked in red, m/z of identified products and the absorbance maximum of Shiff base are marked in blue.

(G) ^{1}H NMR detection of ET isolated from WT and $CSE^{-/-}$ MEF cells incubated with 200 μM ET for 18 h. Experiments were performed in biological triplicates and normalized to the protein content of each sample. Unpaired Student's t test, $^{**}p < 0.01$.

(H) Intracellular levels of homocysteine (HCys), cystathionine (Cysta), and cysteine (Cys) in MEFs treated or not with ET (400 μM) for 2 h, $^{*}p < 0.05$.

(I) Quantification of hercynine formation in N2 and *cth-1 C. elegans* using MALDI imaging MS. Related to the Figure S3R. Unpaired Student's t test, $^{***}p < 0.001$.

CellPress
OPEN ACCESS

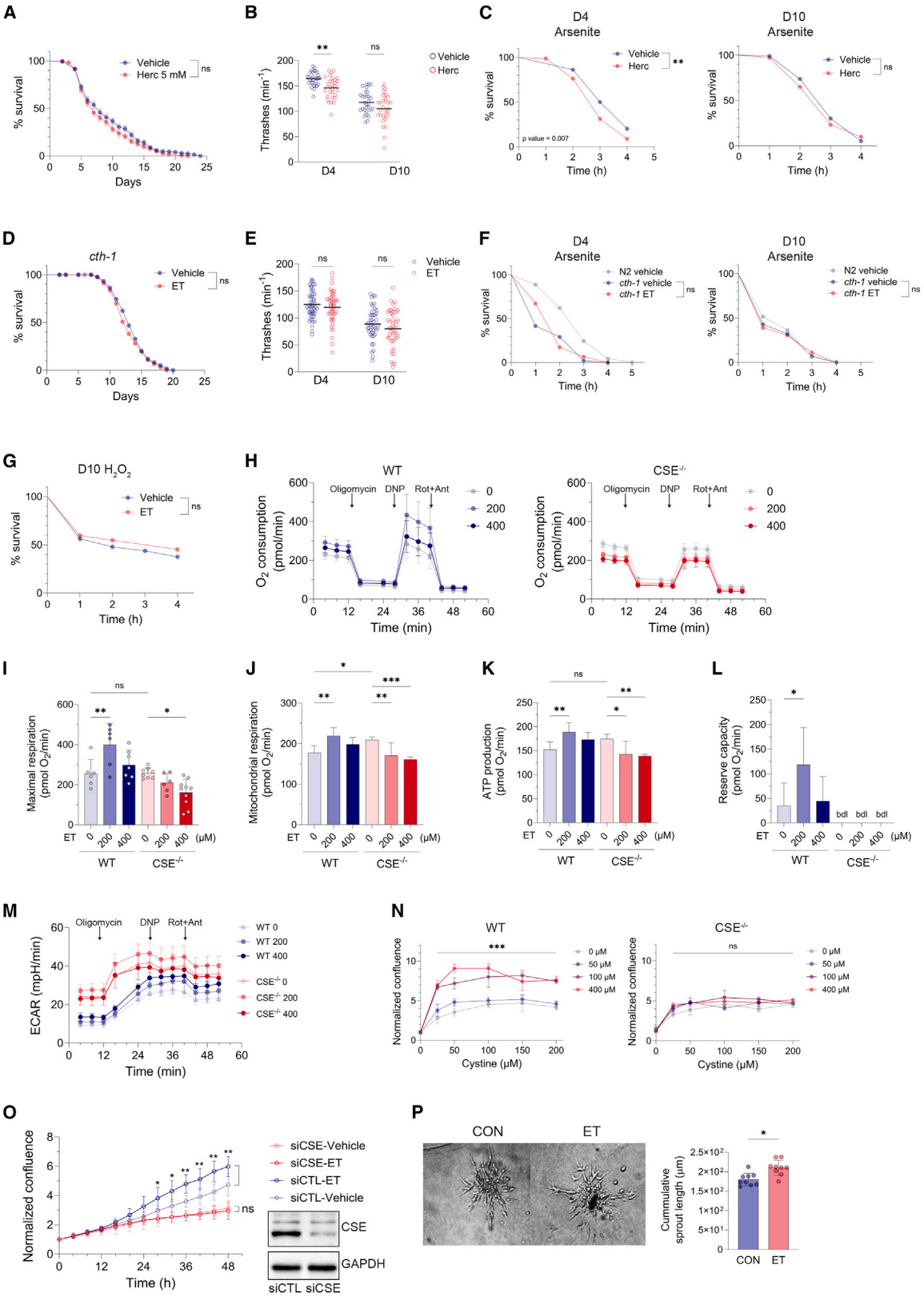

(legend on next page)

suggests that reaction proceeds via initial formation of a carbinolamine adduct (m/z 477.1244; Figure S3I), which forms a Schiff base through loss of water (Figure 2F). When assessed by ^{1}H NMR, the reaction mixture clearly showed formation of a species with $\delta \approx 8$ ppm[32] that corresponds to the aldiminic proton of a Schiff base (Figures S3J and 3K). MS analysis of the reaction mixture after 1 h indicated formation of hercynine as a product of this reaction (Figure S3L).

Formation of hercynine from the Shiff base intermediate is difficult to envision without nucleophilic attack of another thiol (either another molecule of ET or cysteine) (Figure 2F). In that reaction, persulfide would be formed as an intermediate species that will give rise to H_2S.[24] Indeed, ET persulfide could be observed in the MS spectrum of the PLP/ET reaction mixture after 1 h of incubation (Figure S3M). Furthermore, formation of cysteine persulfide could also be observed when cysteine, ET, and PLP were incubated, as confirmed by the characteristic reaction product of 4-chloro-7-nitrobenzofurazan and cysteine persulfide (CysS-S-NBF) adduct[26] that underwent either reduction with beta-mercaptoethanol or switching with dimedone[26] (Figure S3N). Finally, addition of 1,4-dithiothretol (DTT) or tris (2-carboxyethyl)phosphine (TCEP) as a reducing agent, into the reaction mixture of CSE and ET alone, increased the rate of H_2S formation (Figures 2D, S3O, and S3P). The importance of CSE in metabolizing ET was also obvious in the absence of protein persulfidation changes observed in ET-treated CSE$^{-/-}$ cells (Figure S3Q) in contrast to wild-type (WT) cells (Figure S3A).

We next monitored how this reaction affects levels of ET in cells via ^{1}H NMR in WT and CSE$^{-/-}$ MEF cells treated with 200 μM ET. We observed that less ET could be found in WT cells, in accordance with our hypothesis that CSE plays a central role in its metabolism/consumption (Figure 2G). Furthermore, ET treatment did not affect the levels of homocysteine and cystathionine, but significantly higher intracellular levels of cysteine could be observed, in accordance with lower K_m for ET (Figure 2H).

To confirm that ET desulfuration occurs in a CSE-dependent manner in *C. elegans* as well, we adapted matrix-assisted laser desorption/ionization-imaging MS.[33] We could clearly see that product formation is a feature observed in N2 worms and not in *cth-1* mutants (Figure 2I and S3R). Taken together, these data strongly suggested that the beneficial effects of ET are dependent on its consumption by CSE and production of H_2S.

In the light of these observations, we reassessed the ET effects in *C. elegans*. Considering that hercynine is also transported into cells via the same transporter (albeit with lower efficiency),[34] we tested the effect of hercynine. We could observe no significant improvements of *C. elegans* lifespan or healthspan (Figures 3A–3C). This strengthened the claims of ET being responsible for the benefits observed in Figures 1 and S1.

Next, we analyzed the effect of ET on CSE (*cth-1*) mutants. It became immediately apparent that neither lifespan nor motility of worms was affected by ET treatment (Figures 3D and 3E), in contrast to the WT N2 strain (Figures 1B and 1C). Furthermore, the protective effects of ET observed in stress assays performed on WT worms were completely abolished in the *cth-1* mutant (Figures 3F and 3G). This is in accordance with our previous observations that the higher the PSSH levels the better the resistance to stressors.[24] The *cth-1* mutants could not be rescued by the presence of ET alone, as the beneficial effects of ET require CSE to produce H_2S and cause protein persulfidation. Although we did not identify mercaptopyruvate sulfur transferase (MPST) as a target for ET in our thermal proteome profiling of live MEF cells treated with ET (Figure S4A), we did check the effect of ET on healthspan parameters of *mpst-3 C. elegans*. Like in the WT animals, ET treatment improved stress resistance and movement in *mpst-3* mutants (Figures S4B and S4C), akin to other H_2S donors,[26] suggesting that MPST expression is dispensable for ET's beneficial effects.

Next, we tested the role of CSE on the beneficial effects that ET exhibits in cells. ET's antioxidant activity is often claimed to be the main mechanism behind its beneficial effects in different

Figure 3. Lifespan and healthspan benefits of ET treatment are CSE dependent

(A) Lifespan of hercyinine (5 mM)-treated WT (N2) worms (−13% ± 20% for median lifespan, $N \geq 180$ animals per group, Kaplan-Meier survival analysis, Mantel-Cox long rank test; n.s., non-significant).

(B) Movement capacity (the number of thrashing movements made by each worm in 60 s) of aged worms treated with 450 μM hercynine ($N = 30$ per experimental group, two-way ANOVA, $^{**}p < 0.01$).

(C) Survival curves of hercyinine (450 μM)-treated D4 and D10 N2 worms exposed to 5 and 2 mM sodium arsenite, respectively ($N = 80$ for D4 and $N > 100$ for D10; Mantel-Cox long rank test, $^{**}p < 0.01$; n.s., non-significant).

(D) Lifespan of ET (450 μM)-treated *cth-1* mutants (−7.4% ± 0.4% for median lifespan, $N = 260$ animals per group, Kaplan-Meier survival analysis, Mantel-Cox long rank test; n.s., non-significant).

(E) Movement capacity of D10 *cth-1* worms treated with 450 μM ET ($N > 45$ per experimental group, two-way ANOVA, n.s., non-significant).

(F) Survival curves of ET (450 μM)-treated D4 and D10 *cth-1* mutants exposed to 5 and 2 mM sodium arsenite, respectively ($N > 45$ for D4 and $N > 28$ for D10; Mantel-Cox long rank test; n.s., non-significant).

(G) Survival curves of ET (450 μM)-treated D10 *cth-1* mutants exposed to 100 μM H_2O_2 ($N > 42$ per experimental group; Mantel-Cox long rank test; n.s., non-significant).

(H) Real-time mitochondrial respiration, depicted as oxygen consumption rate (OCR), in WT and CSE$^{-/-}$ MEFs treated with 200 and 400 μM ET.

(I–L) Calculated values for respiratory parameters: (I) maximal respiration, (J) mitochondrial respiration, (K) ATP production, and (L) reserve capacity. $n = 6$, two-way ANOVA, $^{*}p < 0.05$, $^{**}p < 0.01$, $^{***}p < 0.001$. bdl, below detection limit.

(M) Extracellular acidification rate (ECAR) in WT and CSE$^{-/-}$ MEFs treated with 200 and 400 μM ET.

(N) Cell proliferation in wild-type (WT, left) and CSE$^{-/-}$ MEFs (right) with the varying concentrations of ET (0–400 μM) and cystine in the medium (0–200 μM). $n = 3$, two-way ANOVA, $^{***}p < 0.001$; n.s., non-significant.

(O) HUVECs were exposed for 48 h in control siRNA (siCTL) or an siRNA directed against CSE (siCSE) and subsequently treated with 100 μM ET. Confluence over time and respective immunoblots for CSE and GAPDH. $n = 6$ biological replicates in technical triplicates. Two-way ANOVA, $^{*}p < 0.05$, $^{**}p < 0.01$; n.s., non-significant.

(P) Representative images and cumulative sprout length of HUVECs treated with 100 μM ET. $n = 3$ biological replicates in technical triplicates. Scale bar, 100 μm. $^{*}p < 0.05$. Paired Student's t test.

CellPress
OPEN ACCESS

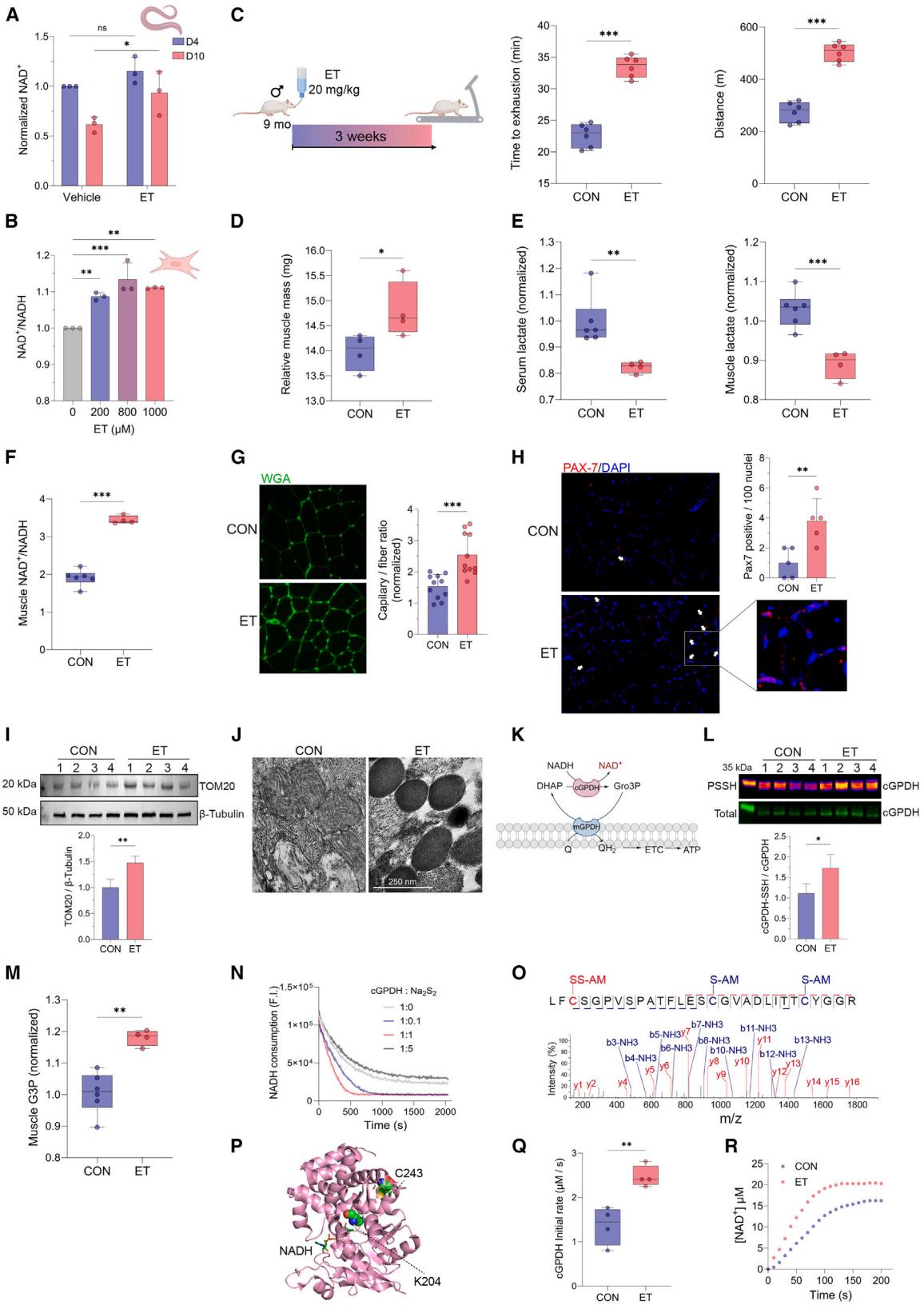

(legend on next page)

studied models.[6,12,35] While ET does prevent H_2O_2-induced cell death (Figure S4D), we find that this effect is CSE dependent (Figures S4E and S4F) and not caused by hercynine alone (Figures S4G and S4H). These data further confirmed that the beneficial effects of ET are not due to its antioxidant activity.

We also assessed the possibility that protective effects might come from the alleged antiferroptotic properties of reactive sulfur species.[36,37] We found no evidence that polysulfide levels change in ET-treated cells nor that ET treatment could prevent erastin and RSL3-induced ferroptotic cell death (Figures S4I and S4J) and lipid peroxidation (Figure S4K).

Depending on the dose, H_2S could act either as a donor of electrons for the electron transport chain (ETC) or as a powerful inhibitor of complex IV.[38] Therefore, we assessed mitochondrial respiration in WT and $CSE^{-/-}$ MEFs treated with ET (Figure 3H). ET treatment caused an increase in maximum respiration (Figure 3I), mitochondrial respiration (basal cellular respiration minus non-mitochondrial respiration; Figure 3J), and ATP production of WT cells (Figure 3K). Basal respiration and non-mitochondrial respiration were also increased (Figures S4L and S4M), as was the reserve respiratory capacity (RRC; maximal respiration minus basal respiration), which tripled (Figure 3L). All these effects were abolished in $CSE^{-/-}$ cells, where ET either had no effect or even reduced the quantified parameters (Figures 3H–3L, S4L, and S4M). Interestingly, the extracellular acidification rate (ECAR) remained unchanged with ET treatment (Figures 3M and S4N). Although our data suggest that $CSE^{-/-}$ cells are highly glycolytic (implying an endogenous role of H_2S), we could observe no further change in glycolytic activity in either WT or $CSE^{-/-}$ cells treated with ET (Figure S4O). This suggests that the ET effects do not come from modulation of glycolytic flux but predominantly from mitochondrial ETC. Furthermore, no change in reduced coenzyme Q (CoQ) levels in cells treated with ET suggests that there is no inhibition of the ETC (Figure S4P).

When energy demand surpasses normal levels, the RRC can step in to boost supply, preventing an "ATP crisis." Higher RRC levels are linked to improved cell survival, whereas lower RRC levels have been linked to cell death and diseases.[39] We next monitored the effect of ET treatment on cell growth. Regardless of the cystine levels in the medium, to provide the substrate for CSE, ET increased the cell growth in a concentration-dependent manner, and this effect was completely abolished in $CSE^{-/-}$ MEFs (Figure 3N). Similar effects could also be observed in human umbilical vein endothelial cells (HUVECs), where silencing of CSE abolished the beneficial effects of ET on cell growth (Figure 3O). It is worth mentioning that these effects are not due to the activation of the mammalian target of rapamycin (mTOR) signaling pathway (Figure S4Q). The ET-treated cells replicate faster due to the activation of the cell cycle, as observed by monitoring the percentage of cells in G2/M phase (Figure S4R; Video S2). This ability of ET to stimulate cell growth of HUVECs (Figure 3O) was also confirmed by their greater sprouting potential (Figure 3P). This is in accordance with recent studies, which also suggested that H_2S somehow stimulates NAD^+ levels in endothelial cells, akin to NAD precursor nicotinamide mononucleotide (NMN), to prevent vascular aging.[40] In fact, most of the observed beneficial effects of ET, such as improvement of lifespan and healthspan, mitochondrial morphology and function, and cell proliferation, could be potentially explained by an increase in NAD^+ levels.[19,41–43]

To understand whether ET treatment affects NAD^+ levels, we first looked at aging *C. elegans*. While aging caused a decline in NAD^+, as previously reported,[19] ET treatment significantly increased those levels (Figure 4A). Similarly, the treatment of MEF cells with ET resulted in a concentration-dependent increase of NAD^+/NADH levels (Figure 4B).

Over the course of aging, NAD^+ levels decrease in various tissues, including skeletal muscle, where clinical evidence underscores age-related NAD^+ deficiency.[19,40,42,44,45] Treatment

Figure 4. Ergothioneine increases the NAD^+ levels and improves the muscle health by causing persulfidation of glycerol 3-phosphate dehydrogenase

(A) NAD^+ levels in *C. elegans* treated with ET (450 μM) until D4 or D10 of adulthood. Two-way ANOVA, $n = 3$, $^*p < 0.05$; n.s., non-significant.

(B) NAD^+/NADH ratios in MEF cells treated with varying concentrations of ET. One-way ANOVA, $n = 3$, $^{**}p < 0.01$, $^{***}p < 0.001$.

(C) 9-month-old male rats were treated with 20 mg/kg ET through drinking water for 3 weeks and subjected to low-intensity test (left). Duration and distance run by rats until exhaustion (right). $N = 6$ per group. Unpaired Student's t test, $^{***}p < 0.001$.

(D) Muscle (*m. gastrocnemius*) mass of rats treated with 20 mg/kg ET through drinking water for 3 weeks. Unpaired Student's t test, $^*p < 0.05$.

(E) Serum (left) and muscle tissue (right) lactate levels. Unpaired Student's t test, $^{**}p < 0.01$, $^{***}p < 0.001$.

(F) NAD^+/NADH levels in rat muscle tissue. Unpaired Student's t test, $^{***}p < 0.001$.

(G) Wheat germ agglutinin (WGA) staining (left) and quantification of blood vessels (right) in muscle tissue sections. 2–3 images per animal were analyzed. $N = 4$. Unpaired Student's t test, $^{***}p < 0.001$.

(H) Representative images of PAX7 (red) immunostained and DAPI (blue) stained muscle tissue sections. Arrows point to PAX7-positive stem cells. Quantification of PAX7-positive stem cells per 100 nuclei is presented. $N = 4$. Unpaired Student's t test, $^{**}p < 0.01$.

(I) Expression levels of mitochondrial TOM20 protein in muscle tissue. $N = 4$. Unpaired Student's t test, $^{**}p < 0.01$.

(J) Representative transmission electron micrographs of ultrathin sections of rat gastrocnemius. Left: control, right: ET-treated. Magnification 15,000×. Scale bar, 250 nm.

(K) Schematic presentation of glycerol-3-phosphate (G3P) shuttle for cytoplasmic NAD^+ generation. cGPDH, cytosolic G3P dehydrogenase; mGPDH, mitochondrial G3P dehydrogenase; ETC, electron transport chain.

(L) Persulfidation levels of cytosolic GPDH in rat muscle tissue. $N = 4$. Unpaired Student's t test, $^*p < 0.05$.

(M) G3P levels in rat muscle tissue. Unpaired Student's t test, $^{**}p < 0.01$.

(N) cGPDH activity of purified enzyme (13.3 nM) pretreated with sodium disulfide (in ratios indicated in the figure) to induce protein persulfidation.

(O) Annotated QExactiveHCD MS/MS spectrum displaying the persulfidated C243 residue in cGPDH.

(P) Ribbon structure of human cGPDH (PDB:1wpq) highlighting the catalytic K204 and C243 as spheres. Solvent-excluded surface of C243 is also shown. Wire model of NADH is also shown.

(Q and R) cGPDH activity (Q: initial reaction rate, R: representative activity recordings) in muscle tissue lysates originating from control or ET-treated rats. UV-vis recording of NADH oxidation was carried out in the presence of 0.2 mM NADH, 0.4 mM dihydroxyacetone phosphate, 7 μM FCCP, and 4 μM rotenone.

with the above-mentioned precursors and supplements improves age-related sarcopenia and muscle performance.[42,46,47] Therefore, we designed the experiment where 9-month-old male rats (*Rattus norvegicus*) were treated with 20 mg/kg ET in drinking water for 3 weeks (Figure 4C) and then subjected to exercise endurance tests. ET-treated animals showed no difference in food and water consumption (Figures S5A and S5B). Both time and distance run to exhaustion were approximately two times higher in ET-treated rats (Figure 4C). 3-week treatment with ET also resulted in significant increases in muscle mass (*m. gastrocnemius*) (Figure 4D) and decreases in post-exercise serum and muscle lactate levels (Figure 4E). On the other hand, pyruvate and oxaloacetate levels were unaffected (Figures S5C and S5D). Most importantly, the treatment resulted in a significant increase of NAD^+/NADH levels in muscle tissue (Figure 4F). While this is consistent with the effects of ET increasing NAD^+ levels in cells and *C. elegans*, it is worth mentioning that neither of the NAD^+ precursors managed to significantly boost NAD^+ levels in muscle, even after much longer supplementation.[3,44,46] Interestingly, ET treatment also affected $NADP^+$/NADPH levels, shifting the equilibrium toward the more reduced form (Figure S5E) and providing the reducing equivalents for the antioxidant defense systems.

NAD^+ has been shown to improve muscular aging by stimulating angiogenesis of blood vessels.[40] As we observed that ET stimulated HUVEC growth and sprouting (Figures 3O and 3P), we compared the vascularization of muscle tissue sections. An obvious increase in total number of blood vessels per muscle fiber was observed (Figure 4G). This was additionally confirmed by detecting higher protein levels of vascular endothelial growth factor (VEGF) receptor in the muscles of animals treated with ET (Figure S5F). It is worth mentioning that, unlike ET, NMN supplementation had no effect on the capillary density of sedentary young to middle-aged mice. Only when coupled with exercise training or after ischemia did NMN improve these parameters.[40]

The maintenance and repair of skeletal muscle rely on dormant muscle stem cells (MuSCs), which become active following muscle injury to proliferate and generate specialized muscle cells, facilitating the regeneration of damaged muscle fibers.[42] With aging, the number and proliferative potential of those MuSCs decreases, but it can be restored by NAD^+ precursors such as nicotinamide riboside (NR),[42] which affects mitochondrial biogenesis. To monitor the effect of ET treatment on MuSC numbers, we stained muscle tissue sections with paired box protein Pax-7 (PAX-7) antibody, a known MuSC marker. Our data show an increase in MuSC number upon ET treatment (Figure 4H), and they also show higher expression levels of mitochondrial import protein Tom 20 (Figure 4I). However, this effect does not appear to be controlled by the changes in sirtuin 1 (SIRT1) or peroxisome proliferator-activated receptor gamma coactivator 1-alpha (PGC1alpha) protein levels (Figure S5G) or by the change of total protein acetylation (Figure S5H). High-electron-density mitochondria were observed in the muscle tissue of ET-treated rats (Figure 4J), characteristic of highly active mitochondria.[48,49]

Taken together, these data support the conclusion that ET treatment boosts NAD^+ levels in treated cells, worms, or rats, which, in turn, acts as a "rejuvenating" agent via mechanisms reported previously.[19,40,42,44,45] The ability of H_2S to increase the NAD^+/NADH ratio and stimulate the subsequent effects akin to NAD^+ precursors has been shown to have beneficial effects on vascular rejuvenation via unidentified mechanisms.[40]

Interestingly, 5-day treatment of both male and female 8-week-old rats with 20 mg/kg ET in the drinking water (Figures S5I–S5K) also resulted in a significant increase in time and distance run to exhaustion (Figures S5L and S5M). Serum levels of NAD^+ in both male and female rats were also significantly higher (Figure S5N), suggesting that metabolic remodeling caused by ET is enough to boost performance of those animals akin to performance-enhancing drugs. ET's ability to boost NAD^+/NADH ratios and muscle mass with short treatment should be explored in the future.

Next, we aimed to understand how ET controls the NAD^+/NADH ratio. One of the main regulators of NAD^+ regeneration in cells is G3P dehydrogenase (GPDH) pathway.[50,51] Because the mitochondrial inner membrane is impermeable to NADH, cells use the G3P shuttle to directly transfer electrons from cytosolic NADH to ETC. Two enzymes, cytosolic (cGPDH) and mitochondrial (mGPDH), maintain this shuttle, with the reaction of cGPDH being the one that generates NAD^+ (Figure 4K). Persulfidome analysis of ET-treated *C. elegans* did find that this pathway is significantly enriched (Figure 1J) and that PSSH levels of cGPDH isoform (GPDH2) are significantly higher without alterations in the protein expression levels (Figure S5O). To test the hypothesis that cGPDH is a regulator of ET's healthspan benefits in *C. elegans*, we treated D4 and D10 *gpdh-1* and *gpdh-2* mutants (those two genes are orthologs of mammalian cGPDH) with ET. ET failed to elicit any improvement in motility (Figure S5P), suggesting that ET-induced protein persulfidation of this enzyme might be the key reason for the observed boosting of NAD^+ levels.

Using the dimedone-switch method for persulfide labeling, we also observed that ET treatment induced a significant increase in the persulfidation of GPDH in rat muscle (Figure 4L). This was further followed by an increase in G3P levels, which suggested that PSSH of GPDH might be increasing the enzyme's activity (Figure 4M). To address this, we used purified cGPDH and treated it with sodium disulfide (Na_2S_2). Mammalian cGPDH contains 11 cysteines (Figure S5Q). Therefore, we incubated cGPDH with varying concentrations of Na_2S_2 and measured the enzyme activity (conversion of NADH to NAD^+ upon addition of dihydroxyacetone phosphate as a substrate). We observed that the disulfide-to-protein ratios up to 1:1 resulted in a significant increase in enzyme activity (k_{obs} = 1.8 × 10^{-3} s^{-1} for untreated vs. 3.6 x 10^{-3} s^{-1} for persulfidated), while higher ratios (expected to modify more than one cysteine) did not significantly affect the activity (Figure 4N). In order to identify which cysteine is undergoing persulfidation, we subjected the samples to liquid chromatography-tandem mass spectrometry (LC-MS/MS). Our data show that cysteine 243 is the main target for protein persulfidation (Figure 4O). Analyzing the crystal structure of human GPD, it becomes apparent that C243, located at the beginning of a beta strand, is surface exposed (Figure 4P) and therefore easily available for the reaction. Although significantly far away from the active site K204 (Figure 4P), mutational studies of distant regions have been shown to change the conformation of catalytic loop 292–297 leading to the increase of GPD activity.[52] Indeed, when we assessed the activity of cGPDH in the lysates of muscle

tissue from untreated and ET-treated rats (experiments require a full inhibition of mitochondrial respiration to prevent the contribution of the mGPDH part of the shuttle),[53] we could detect an ~2-fold increase in enzyme activity (Figures 4Q and 4R).

DISCUSSION

Through a series of experiments utilizing *C. elegans*, mammalian cell lines, and animal models, we have elucidated the molecular pathways underlying ET's beneficial effects, with implications for translational research and therapeutic development. Our findings highlight the pivotal role of CSE in mediating the beneficial effects of ET. The absence of CSE abolishes ET's protective effects, emphasizing the essential role of H_2S signaling in ET-induced metabolic resilience. This aligns with recent studies emphasizing CSE as one of the few pro-longevity genes universally upregulated in various lifespan extension interventions.[16,54]

Given that ET accumulates in high concentrations due to the presence of the organic cation membrane transporter OCTN-1,[34] the low mM K_m for ET that we observed suggests that it could serve as a preferred substrate over cysteine, resulting in increased H_2S production. H_2S has been shown to stimulate respiration and cell proliferation[55,56] and it also extends lifespan and improves healthspan of *C. elegans*,[57–59] effects similar to those we observed for ET. These benefits are not only due to modulation of respiration but also involve the widespread increase of protein persulfidation, which is an evolutionarily conserved modification that rescues cysteines from hyperoxidation.[26,60] Indeed, ET increases protein persulfidation, maintaining high levels even at D10 *C. elegans*. These findings align with recent observations that increased persulfidation correlates with enhanced resistance to stress.[26] Although we cannot rule out that ET acts as a direct scavenger or reactive oxygen species, our results suggest that its direct antioxidant action is not a primary mechanism for its beneficial effects, as previously proposed.[61]

Beyond global protection, protein persulfidation also serves as a regulatory posttranslational modification.[25] One of the key targets of CSE-catalyzed, ET-induced persulfidation is cGPDH. cGPDH emerges as a key regulator of NAD^+/NADH homeostasis, potentially ameliorating mitochondrial disease.[50,51] Its posttranslational modification, such as phosphorylation, has been reported in the skeletal muscle of hibernating ground squirrels.[62] Our findings in cells, *C. elegans*, and aging rats suggest that persulfidation of cGPDH enhances its activity, leading to an increase in NAD^+ levels. Notably, ET fails to elicit healthspan benefits in *C. elegans* lacking cGPDH.

NAD^+ is a crucial coenzyme, vital for cellular and organismal metabolism, stemming from precursors within the vitamin B_3 family.[41] Mammals possess the capability to generate NAD^+ from various dietary sources, such as NR, NMN, and trigonelline.[3,41,43] Supplementation with these compounds improves age-related sarcopenia and muscle performance.[42,46,47] Our data suggest that the effects of ET on aged *C. elegans* and aged rats are comparable with, if not more efficient than, those of NAD^+ precursors (NR, NMN, and trigonelline). This is consistent with observations in mice.[14,63] Interestingly, H_2S has been shown to boost NAD^+, thereby improving muscle aging by stimulating angiogenesis.[40] The CSE-H_2S-cGPDH-SSH-NAD^+ pathway we describe for ET could therefore account for the full range of beneficial effects observed in rats, including increased vascularization, muscle mass, and stem cell number, as well as improved mitochondrial morphology and better physical endurance. While some of those effects (such as improvement of mitochondrial morphology in both *C. elegans* and rats, as well as MuSCs count) suggest a rejuvenating action of ET, the performance-improving effects observed with short-term ET exposure (5 days) imply that metabolic remodeling induced by this pathway could also be exploited for performance enhancement.

In conclusion, by unraveling the molecular intricacies of ET's actions, our research lays the groundwork for further exploration of its clinical applications and therapeutic implications. Future studies may explore the therapeutic potential of ET in mitigating age-related conditions and metabolic disorders, with a focus on translational approaches aimed at harnessing its rejuvenating properties for human health. Finally, recently reported edible mycelium, bioengineered to boost both nutritional value and ET levels,[64] holds promise as a potential future source to augment daily ET intake.

Limitations of the study

Although holding great promise for healthspan improvements in humans, it is worth stating that ET's beneficial effects might be reduced at much older ages due to reported age-induced decline in CSE expression.[26] A combination of ET with the activators of CSE expression might be a therapeutic avenue to overcome those issues. Furthermore, several mutations that lead to partial or full inactivation of CSE have been described in humans,[65] so ET supplementation can fail to elicit the beneficial effects in those individuals. Finally, being readily accumulated in the cells, the amount of consumed ET and the expression levels of CSE will define whether the toxic threshold of H_2S production is achieved.

RESOURCE AVAILABILITY

Lead contact

Further information and requests for resources and reagents should be directed to, and will be fulfilled by, the lead contact, Milos R. Filipovic (milos.filipovic@glasgow.ac.uk).

Materials availability

This study did not generate any new reagents.

Data and code availability

- The MS proteomics data have been deposited to the ProteomeXchange Consortium via the PRIDE partner repository with the dataset identifier PXD051587 and PXD051609.
- RNA-seq data have been deposited to the BioProject database, with the BioProject ID PRJNA1178314.
- Original western blot and gel images and unprocessed data used for creating graphs in Figures 1, 2, 3, 4, S1, S4, and S5 are available as PDF and Excel spread sheets in Data S1 – source data.
- This paper does not report original code.
- Any additional information required to reanalyze the data reported in this paper is available from the lead contact upon request.

ACKNOWLEDGMENTS

We thank Prof. Beatriz Alvarez (University of Uruguay) for helpful discussions about PLP/ET mechanisms, Prof. Bindu Paul (Johns Hopkins University) for

CellPress
OPEN ACCESS

$CSE^{-/-}$ and MEFs, Prof. Ruma Banarjee (University of Michigan) for human recombinant CSE, and Ingo Feldman and Susanne Krois (ISAS e.V.) for technical assistance with MS and help with metabolomic analysis of amino acids.

This study was funded by the European Research Council (ERC) under the European Union's Horizon 2020 research and innovation programme (grant agreement No. 864921). V.O., A.S., N.S., J.Z., and M.M. acknowledge support from The Ministry of Science, Technological Development and Innovation of the Republic of Serbia (contract no. 451-03-47/2023-01/200007). M.P.M. acknowledges support by the Medical Research Council UK (MC_UU_00028/4) and by a Wellcome Trust Investigator award (220257/Z/20/Z). S.I.B. was supported by the Deutsche Forschungsgemeinschaft (Emmy Noether Program BI 2163/1-1). M.K.D. was supported with a scholarship from Onassis Foundation.

AUTHOR CONTRIBUTIONS

M.R.F. conceived the study. D.P., L.S., and Y.P. performed all *C. elegans* experiments. D.P. and D.D.'A. performed all MEF cell experiments. D.P. performed all proteomics, purified protein, and enzymology experiments. T.V. performed thermal proteome profiling. J.L.M., A.M.C., and C.Y. performed the analysis of intracellular H_2S production, CoQ levels, and LC-MS detection of hercynine. V.M.J. performed bioinformatic analysis of RNA-seq data and M.K.D. performed the HUVEC experiments. N. Savic, A.S., D.M., N. Sutulovic, and V.O. performed experiments on rats. Seahorse analysis of mitochondrial function was performed by A.R. and M.V.-L., MALDI imaging and amino acid quantification by LC-MS was done by K.W.S. and P.P., and ET detection by NMR was performed by A.K.-Y. and R.H. M.K. did NMR detection of the PLP reaction. J.Z. and M.M. performed TEM. M.S., A.M.-V., O.S., I.I.-B., M.V.-L., S.-I.B., M.P.M., and V.O. also provided tools and intellectual input and helped with data analysis. M.R.F. wrote the manuscript with the help of all co-authors.

DECLARATION OF INTERESTS

The authors declare no competing interests.

STAR★METHODS

Detailed methods are provided in the online version of this paper and include the following:

- KEY RESOURCES TABLE
- EXPERIMENTAL MODELS AND SUBJECT DETAILS
  - *C. elegans*
  - Cell lines
  - Wistar rats
- METHOD DETAILS
  - C. elegans experiments
  - Cell experiments
  - Biochemical experiments
  - Experiments with rats
- QUANTIFICATION AND STATISTICAL ANALYSIS

SUPPLEMENTAL INFORMATION

Supplemental information can be found online at https://doi.org/10.1016/j.cmet.2024.12.008.

Received: April 23, 2024
Revised: September 22, 2024
Accepted: December 17, 2024
Published: January 21, 2025

REFERENCES

1. D'Amico, D., Andreux, P.A., Valdés, P., Singh, A., Rinsch, C., and Auwerx, J. (2021). Impact of the Natural Compound Urolithin A on Health, Disease, and Aging. Trends Mol. Med. *27*, 687–699. https://doi.org/10.1016/j.molmed.2021.04.009.
2. Madeo, F., Eisenberg, T., Pietrocola, F., and Kroemer, G. (2018). Spermidine in health and disease. Science *359*, eaan2788. https://doi.org/10.1126/science.aan2788.
3. Membrez, M., Migliavacca, E., Christen, S., Yaku, K., Trieu, J., Lee, A.K., Morandini, F., Giner, M.P., Stiner, J., Makarov, M.V., et al. (2024). Trigonelline is an NAD^+ precursor that improves muscle function during ageing and is reduced in human sarcopenia. Nat. Metab. *6*, 433–447. https://doi.org/10.1038/s42255-024-00997-x.
4. Singh, P., Gollapalli, K., Mangiola, S., Schranner, D., Yusuf, M.A., Chamoli, M., Shi, S.L., Bastos, B.L., Nair, T., Riermeier, A., et al. (2023). Taurine deficiency as a driver of aging. Science *380*, eabn9257. https://doi.org/10.1126/science.abn9257.
5. Tian, X., Thorne, J.L., and Moore, J.B. (2023). Ergothioneine: An underrecognised dietary micronutrient required for healthy ageing? Br. J. Nutr. *129*, 104–114. https://doi.org/10.1017/S0007114522003592.
6. Cheah, I.K., and Halliwell, B. (2012). Ergothioneine; antioxidant potential, physiological function and role in disease. Biochim. Biophys. Acta *1822*, 784–793. https://doi.org/10.1016/j.bbadis.2011.09.017.
7. Cheah, I.K., and Halliwell, B. (2021). Ergothioneine, recent developments. Redox Biol. *42*, 101868. https://doi.org/10.1016/j.redox.2021.101868.
8. Paul, B.D. (2022). Ergothioneine: A Stress Vitamin with Antiaging, Vascular, and Neuroprotective Roles? Antioxid. Redox Signal. *36*, 1306–1317. https://doi.org/10.1089/ars.2021.0043.
9. Halliwell, B., and Cheah, I. (2024). Are age-related neurodegenerative diseases caused by a lack of the diet-derived compound ergothioneine? Free Radic. Biol. Med. *217*, 60–67. https://doi.org/10.1016/j.freeradbiomed.2024.03.009.
10. Tucker, R.A.J., Cheah, I.K., and Halliwell, B. (2019). Specificity of the ergothioneine transporter natively expressed in HeLa cells. Biochem. Biophys. Res. Commun. *513*, 22–27. https://doi.org/10.1016/j.bbrc.2019.02.122.
11. Cheah, I.K., Ong, R.L.S., Gruber, J., Yew, T.S.K., Ng, L.F., Chen, C.B., and Halliwell, B. (2013). Knockout of a putative ergothioneine transporter in Caenorhabditis elegans decreases lifespan and increases susceptibility to oxidative damage. Free Radic. Res. *47*, 1036–1045. https://doi.org/10.3109/10715762.2013.848354.
12. Akanmu, D., Cecchini, R., Aruoma, O.I., and Halliwell, B. (1991). The antioxidant action of ergothioneine. Arch. Biochem. Biophys. *288*, 10–16. https://doi.org/10.1016/0003-9861(91)90158-F.
13. Van Laer, K., Hamilton, C.J., and Messens, J. (2013). Low-molecular-weight thiols in thiol-disulfide exchange. Antioxid. Redox Signal. *18*, 1642–1653. https://doi.org/10.1089/ars.2012.4964.
14. Katsube, M., Ishimoto, T., Fukushima, Y., Kagami, A., Shuto, T., and Kato, Y. (2024). Ergothioneine promotes longevity and healthy aging in male mice. GeroScience *46*, 3889–3909. https://doi.org/10.1007/s11357-024-01111-5.
15. Wu, L.Y., Kan, C.N., Cheah, I.K., Chong, J.R., Xu, X., Vrooman, H., Hilal, S., Venketasubramanian, N., Chen, C.P., Halliwell, B., et al. (2022). Low Plasma Ergothioneine Predicts Cognitive and Functional Decline in an Elderly Cohort Attending Memory Clinics. Antioxidants (Basel) *11*, 1717. https://doi.org/10.3390/antiox11091717.
16. Tyshkovskiy, A., Bozaykut, P., Borodinova, A.A., Gerashchenko, M.V., Ables, G.P., Garratt, M., Khaitovich, P., Clish, C.B., Miller, R.A., and Gladyshev, V.N. (2019). Identification and Application of Gene Expression Signatures Associated with Lifespan Extension. Cell Metab. *30*, 573–593.e8. https://doi.org/10.1016/j.cmet.2019.06.018.
17. Bansal, A., Zhu, L.J., Yen, K., and Tissenbaum, H.A. (2015). Uncoupling lifespan and healthspan in caenorhabditis elegans longevity mutants. Proc. Natl. Acad. Sci. USA *112*, E277–E286. https://doi.org/10.1073/pnas.1412192112.
18. Pincus, Z., Mazer, T.C., and Slack, F.J. (2016). Autofluorescence as a measure of senescence in C. elegans: Look to red, not blue or green. Aging *8*, 889–898. https://doi.org/10.18632/aging.100936.
19. Mouchiroud, L., Houtkooper, R.H., Moullan, N., Katsyuba, E., Ryu, D., Cantó, C., Mottis, A., Jo, Y.S., Viswanathan, M., Schoonjans, K., et al.

(2013). XThe NAD+/sirtuin pathway modulates longevity through activation of mitochondrial UPR and FOXO signaling. Cell *154*, 430–441. https://doi.org/10.1016/j.cell.2013.06.016.

20. Narayan, V., Ly, T., Pourkarimi, E., Murillo, A.B., Gartner, A., Lamond, A.I., and Kenyon, C. (2016). Deep Proteome Analysis Identifies Age-Related Processes in C. elegans. Cell Syst. *3*, 144–159. https://doi.org/10.1016/j.cels.2016.06.011.
21. Walther, D.M., Kasturi, P., Zheng, M., Pinkert, S., Vecchi, G., Ciryam, P., Morimoto, R.I., Dobson, C.M., Vendruscolo, M., Mann, M., et al. (2015). Widespread proteome remodeling and aggregation in aging C. elegans. Cell *161*, 919–932. https://doi.org/10.1016/j.cell.2015.03.032.
22. Zaorska, E., Hutsch, T., Gawryś-Kopczyńska, M., Ostaszewski, R., Ufnal, M., and Koszelewski, D. (2019). Evaluation of thioamides, thiolactams and thioureas as hydrogen sulfide (H2S) donors for lowering blood pressure. Bioorg. Chem. *88*, 102941. https://doi.org/10.1016/j.bioorg.2019.102941.
23. Wang, Z.D., Yoshida, M., and George, B. (2013). Theoretical study on the thermal decomposition of thiourea. Comput. Theor. Chem. *1017*, 91–98. https://doi.org/10.1016/j.comptc.2013.05.007.
24. Filipovic, M.R., Zivanovic, J., Alvarez, B., and Banerjee, R. (2018). Chemical Biology of H2S Signaling through Persulfidation. Chem. Rev. *118*, 1253–1337. https://doi.org/10.1021/acs.chemrev.7b00205.
25. Vignane, T., and Filipovic, M.R. (2023). Emerging Chemical Biology of Protein Persulfidation. Antioxid. Redox Signal. *39*, 19–39. https://doi.org/10.1089/ars.2023.0352.
26. Zivanovic, J., Kouroussis, E., Kohl, J.B., Adhikari, B., Bursac, B., Schott-Roux, S., Petrovic, D., Miljkovic, J.L., Thomas-Lopez, D., Jung, Y., et al. (2019). Selective Persulfide Detection Reveals Evolutionarily Conserved Antiaging Effects of S-Sulfhydration. Cell Metab. *30*, 1152–1170.e13. https://doi.org/10.1016/j.cmet.2019.10.007.
27. Savitski, M.M., Reinhard, F.B.M., Franken, H., Werner, T., Savitski, M.F., Eberhard, D., Martinez Molina, D., Jafari, R., Dovega, R.B., Klaeger, S., et al. (2014). Tracking cancer drugs in living cells by thermal profiling of the proteome. Science *346*, 1255784. https://doi.org/10.1126/science.1255784.
28. Perrin, J., Werner, T., Kurzawa, N., Rutkowska, A., Childs, D.D., Kalxdorf, M., Poeckel, D., Stonehouse, E., Strohmer, K., Heller, B., et al. (2020). Identifying drug targets in tissues and whole blood with thermal-shift profiling. Nat. Biotechnol. *38*, 303–308. https://doi.org/10.1038/s41587-019-0388-4.
29. Murail, S., de Vries, S.J., Rey, J., Moroy, G., and Tufféry, P. (2021). SeamDock: An Interactive and Collaborative Online Docking Resource to Assist Small Compound Molecular Docking. Front. Mol. Biosci. *8*, 716466. https://doi.org/10.3389/fmolb.2021.716466.
30. Chiku, T., Padovani, D., Zhu, W., Singh, S., Vitvitsky, V., and Banerjee, R. (2009). H2S Biogenesis by Human Cystathionine gamma-Lyase Leads to the Novel Sulfur Metabolites Lanthionine and Homolanthionine and Is Responsive to the Grade of Hyperhomocysteinemia. J. Biol. Chem. *284*, 11601–11612. https://doi.org/10.1074/jbc.M808026200.
31. Carlsson, J., Kierstan, M.P.J., and Brocklehurst, K. (1974). Reactions of L-ergothioneine and some other aminothiones with 2,2′- and 4,4′- dipyridyl disulphides and of L-ergothioneine with iodoacetamide. 2-Mercaptoimidazoles, 2- and 4-thiopyridones, thiourea and thioacetamide as highly reactive neutral sulphur nucleop. Biochem. J. *139*, 221–235. https://doi.org/10.1042/bj1390221.
32. Mulay, P., Chen, C., and Krishna, V. (2023). Enzyme-independent catabolism of cysteine with pyridoxal-5′-phosphate. Sci. Rep. *13*, 312. https://doi.org/10.1038/s41598-022-26966-6.
33. Hameed, S., Ikegami, K., Sugiyama, E., Matsushita, S., Kimura, Y., Hayasaka, T., Sugiura, Y., Masaki, N., Waki, M., Ohta, I., et al. (2015). Direct profiling of the phospholipid composition of adult Caenorhabditis elegans using whole-body imaging mass spectrometry. Anal. Bioanal. Chem. *407*, 7589–7602. https://doi.org/10.1007/s00216-015-8932-7.
34. Gründemann, D., Hartmann, L., and Flögel, S. (2022). The ergothioneine transporter (ETT): substrates and locations, an inventory. FEBS Lett. *596*, 1252–1269. https://doi.org/10.1002/1873-3468.14269.
35. Paul, B.D., and Snyder, S.H. (2010). The unusual amino acid L-ergothioneine is a physiologic cytoprotectant. Cell Death Differ. *17*, 1134–1140. https://doi.org/10.1038/cdd.2009.163.
36. Barayeu, U., Schilling, D., Eid, M., Xavier da Silva, T.N., Schlicker, L., Mitreska, N., Zapp, C., Gräter, F., Miller, A.K., Kappl, R., et al. (2023). Hydropersulfides inhibit lipid peroxidation and ferroptosis by scavenging radicals. Nat. Chem. Biol. *19*, 28–37. https://doi.org/10.1038/s41589-022-01145-w.
37. Wu, Z., Khodade, V.S., Chauvin, J.R., Rodriguez, D., Toscano, J.P., and Pratt, D.A. (2022). Hydropersulfides Inhibit Lipid Peroxidation and Protect Cells from Ferroptosis. J. Am. Chem. Soc. *144*, 15825–15837. https://doi.org/10.1021/jacs.2c06804.
38. Hanna, D., Kumar, R., and Banerjee, R. (2023). A Metabolic Paradigm for Hydrogen Sulfide Signaling via Electron Transport Chain Plasticity. Antioxid. Redox Signal. *38*, 57–67. https://doi.org/10.1089/ARS.2022.0067.
39. Pfleger, J., He, M., and Abdellatif, M. (2015). Mitochondrial complex II is a source of the reserve respiratory capacity that is regulated by metabolic sensors and promotes cell survival. Cell Death Dis. *6*, e1835. https://doi.org/10.1038/cddis.2015.202.
40. Das, A., Huang, G.X., Bonkowski, M.S., Longchamp, A., Li, C., Schultz, M.B., Kim, L.J., Osborne, B., Joshi, S., Lu, Y., et al. (2018). Impairment of an Endothelial NAD+-H2S Signaling Network Is a Reversible Cause of Vascular Aging. Cell *173*, 74–89.e20. https://doi.org/10.1016/j.cell.2018.02.008.
41. Verdin, E. (2015). NAD+ in aging, metabolism, and neurodegeneration. Science *350*, 1208–1213. https://doi.org/10.1126/science.aac4854.
42. Zhang, H., Ryu, D., Wu, Y., Gariani, K., Wang, X., Luan, P., D'Amico, D., Ropelle, E.R., Lutolf, M.P., Aebersold, R., et al. (2016). NAD+ repletion improves mitochondrial and stem cell function and enhances life span in mice. Science *352*, 1436–1443. https://doi.org/10.1126/science.aaf2693.
43. Yaku, K., Okabe, K., and Nakagawa, T. (2018). NAD metabolism: Implications in aging and longevity. Ageing Res. Rev. *47*, 1–17. https://doi.org/10.1016/j.arr.2018.05.006.
44. Ryu, D., Zhang, H., Ropelle, E.R., Sorrentino, V., Mázala, D.A.G., Mouchiroud, L., Marshall, P.L., Campbell, M.D., Ali, A.S., Knowels, G.M., et al. (2016). NAD+ repletion improves muscle function in muscular dystrophy and counters global parylation. Sci. Transl. Med. *8*, 361ra139. https://doi.org/10.1126/scitranslmed.aaf5504.
45. Gomes, A.P., Price, N.L., Ling, A.J.Y., Moslehi, J.J., Montgomery, M.K., Rajman, L., White, J.P., Teodoro, J.S., Wrann, C.D., Hubbard, B.P., et al. (2013). Declining NAD+ induces a pseudohypoxic state disrupting nuclear-mitochondrial communication during aging. Cell *155*, 1624–1638. https://doi.org/10.1016/j.cell.2013.11.037.
46. Mills, K.F., Yoshida, S., Stein, L.R., Grozio, A., Kubota, S., Sasaki, Y., Redpath, P., Migaud, M.E., Apte, R.S., Uchida, K., et al. (2016). Long-Term Administration of Nicotinamide Mononucleotide Mitigates Age-Associated Physiological Decline in Mice. Cell Metab. *24*, 795–806. https://doi.org/10.1016/j.cmet.2016.09.013.
47. Yoshino, J., Baur, J.A., and Imai, S.I. (2018). NAD+ Intermediates: The Biology and Therapeutic Potential of NMN and NR. Cell Metab. *27*, 513–528. https://doi.org/10.1016/j.cmet.2017.11.002.
48. Jiang, Y.F., Lin, S.S., Chen, J.M., Tsai, H.Z., Hsieh, T.S., and Fu, C.Y. (2017). Electron tomographic analysis reveals ultrastructural features of mitochondrial cristae architecture which reflect energetic state and aging. Sci. Rep. *7*, 45474. https://doi.org/10.1038/srep45474.
49. Picard, M., White, K., and Turnbull, D.M. (2013). Mitochondrial morphology, topology, and membrane interactions in skeletal muscle: a quantitative three-dimensional electron microscopy study. J. Appl. Physiol. *114*, 161–171. https://doi.org/10.1152/japplphysiol.01096.2012.
50. Mithal, D.S., and Chandel, N.S. (2021). The Gro3p factor: restoring NAD+/NADH homeostasis to ameliorate mitochondrial disease. Cell Metab. *33*, 1905–1907. https://doi.org/10.1016/j.cmet.2021.09.006.

51. Liu, S., Fu, S., Wang, G., Cao, Y., Li, L., Li, X., Yang, J., Li, N., Shan, Y., Cao, Y., et al. (2021). Glycerol-3-phosphate biosynthesis regenerates cytosolic NAD^+ to alleviate mitochondrial disease. Cell Metab. *33*, 1974–1987.e9. https://doi.org/10.1016/j.cmet.2021.06.013.

52. Mhashal, A.R., Romero-Rivera, A., Mydy, L.S., Cristobal, J.R., Gulick, A.M., Richard, J.P., and Kamerlin, S.C.L. (2020). Modeling the Role of a Flexible Loop and Active Site Side Chains in Hydride Transfer Catalyzed by Glycerol-3-phosphate Dehydrogenase. ACS Catal. *10*, 11253–11267. https://doi.org/10.1021/acscatal.0c02757.

53. Houštěk, J., Cannon, B., and Lindberg, O. (1975). Glycerol-3-Phosphate Shuttle and Its Function in Intermediary Metabolism of Hamster Brown-Adipose Tissue. Eur. J. Biochem. *54*, 11–18. https://doi.org/10.1111/j.1432-1033.1975.tb04107.x.

54. Tyshkovskiy, A., Ma, S., Shindyapina, A.V., Tikhonov, S., Lee, S.-G., Bozaykut, P., Castro, J.P., Seluanov, A., Schork, N.J., Gorbunova, V., et al. (2023). Distinct longevity mechanisms across and within species and their association with aging. Cell *186*, 2929–2949.e20. https://doi.org/10.1016/j.cell.2023.05.002.

55. Szabo, C., Ransy, C., Módis, K., Andriamihaja, M., Murghes, B., Coletta, C., Olah, G., Yanagi, K., and Bouillaud, F. (2014). Regulation of mitochondrial bioenergetic function by hydrogen sulfide. Part I. Biochemical and physiological mechanisms *171*, 2099–2122. https://doi.org/10.1111/bph.12369.

56. Hanna, D.A., Diessl, J., Guha, A., Kumar, R., Andren, A., Lyssiotis, C., and Banerjee, R. (2024). H2S preconditioning induces long-lived perturbations in O2 metabolism. Proc. Natl. Acad. Sci. USA *121*, e2319473121. https://doi.org/10.1073/pnas.2319473121.

57. Miller, D.L., and Roth, M.B. (2007). Hydrogen sulfide increases thermotolerance and lifespan in Caenorhabditis elegans. Proc. Natl. Acad. Sci. USA *104*, 20618–20622. https://doi.org/10.1073/pnas.0710191104.

58. Qabazard, B., Li, L., Gruber, J., Peh, M.T., Ng, L.F., Kumar, S.D., Rose, P., Tan, C.-H., Dymock, B.W., Wei, F., et al. (2014). Hydrogen Sulfide Is an Endogenous Regulator of Aging in Caenorhabditis elegans. Antioxid. Redox Signal. *20*, 2621–2630. https://doi.org/10.1089/ars.2013.5448.

59. Ng, L.T., Ng, L.F., Tang, R.M.Y., Barardo, D., Halliwell, B., Moore, P.K., and Gruber, J. (2020). Lifespan and healthspan benefits of exogenous H2S in C. elegans are independent from effects downstream of eat-2 mutation. npj Aging Mech. Dis. *6*, 6. https://doi.org/10.1038/s41514-020-0044-8.

60. Dóka, É., Ida, T., Dagnell, M., Abiko, Y., Luong, N.C., Balog, N., Takata, T., Espinosa, B., Nishimura, A., Cheng, Q., et al. (2020). Control of protein function through oxidation and reduction of persulfidated states. Sci. Adv. *6*, eaax8358. https://doi.org/10.1126/sciadv.aax8358.

61. Halliwell, B., Tang, R.M.Y., and Cheah, I.K. (2023). Diet-Derived Antioxidants: The Special Case of Ergothioneine. Annu. Rev. Food Sci. Technol. *14*, 323–345. https://doi.org/10.1146/annurev-food-060822-122236.

62. Ruberto, A.A., Logan, S.M., and Storey, K.B. (2019). Temperature and serine phosphorylation regulate glycerol-3-phosphate dehydrogenase in skeletal muscle of hibernating Richardson's ground squirrels. Biochem. Cell Biol. *97*, 148–157. https://doi.org/10.1139/bcb-2018-0198.

63. Fovet, T., Guilhot, C., Delobel, P., Chopard, A., Py, G., and Brioche, T. (2022). Ergothioneine Improves Aerobic Performance Without Any Negative Effect on Early Muscle Recovery Signaling in Response to Acute Exercise. Front. Physiol. *13*, 834597. https://doi.org/10.3389/fphys.2022.834597.

64. Maini Rekdal, V., van der Luijt, C.R.B., Chen, Y., Kakumanu, R., Baidoo, E.E.K., Petzold, C.J., Cruz-Morales, P., and Keasling, J.D. (2024). Edible mycelium bioengineered for enhanced nutritional value and sensory appeal using a modular synthetic biology toolkit. Nat. Commun. *15*, 2099. https://doi.org/10.1038/s41467-024-46314-8.

65. Kraus, J.P., Hašek, J., Kožich, V., Collard, R., Venezia, S., Janošíková, B., Wang, J., Stabler, S.P., Allen, R.H., Jakobs, C., et al. (2009). Cystathionine γ-lyase:, metabolic, genetic, and structural studies. Mol. Genet. Metab. *97*, 250–259. https://doi.org/10.1016/j.ymgme.2009.04.001.

66. Hu, J., Leisegang, M.S., Looso, M., Drekolia, M.-K., Wittig, J., Mettner, J., Karantanou, C., Kyselova, A., Dumbović, G., Li, X., et al. (2023). Disrupted Binding of Cystathionine γ-Lyase to p53 Promotes Endothelial Senescence. Circ. Res. *133*, 842–857. https://doi.org/10.1161/CIRCRESAHA.123.323084.

67. Wedmann, R., Onderka, C., Wei, S., Szijártó, I.A., Miljkovic, J.L., Mitrovic, A., Lange, M., Savitsky, S., Yadav, P.K., Torregrossa, R., et al. (2016). Improved tag-switch method reveals that thioredoxin acts as depersulfidase and controls the intracellular levels of protein persulfidation. Chem. Sci. *7*, 3414–3426. https://doi.org/10.1039/c5sc04818d.

68. Sbodio, J.I., Snyder, S.H., and Paul, B.D. (2016). Transcriptional control of amino acid homeostasis is disrupted in Huntington's disease. Proc. Natl. Acad. Sci. USA *113*, 8843–8848. https://doi.org/10.1073/pnas.1608264113.

69. Schneider, C.A., Rasband, W.S., and Eliceiri, K.W. (2012). NIH Image to ImageJ: 25 years of image analysis. Nat. Methods *9*, 671–675. https://doi.org/10.1038/nmeth.2089.

70. Hulsen, T., de Vlieg, J., and Alkema, W. (2008). BioVenn – a web application for the comparison and visualization of biological lists using area-proportional Venn diagrams. BMC Genomics *9*, 488. https://doi.org/10.1186/1471-2164-9-488.

71. Kong, A.T., Leprevost, F.V., Avtonomov, D.M., Mellacheruvu, D., and Nesvizhskii, A.I. (2017). MSFragger: Ultrafast and comprehensive peptide identification in mass spectrometry-based proteomics. Nat. Methods *14*, 513–520. https://doi.org/10.1038/nmeth.4256.

72. Huang, D.W., Sherman, B.T., and Lempicki, R.A. (2009). Systematic and integrative analysis of large gene lists using David bioinformatics resources. Nat. Protoc. *4*, 44–57. https://doi.org/10.1038/nprot.2008.211.

73. Karpievitch, Y.V., Taverner, T., Adkins, J.N., Callister, S.J., Anderson, G.A., Smith, R.D., and Dabney, A.R. (2009). Normalization of peak intensities in bottom-up MS-based proteomics using singular value decomposition. Bioinformatics *25*, 2573–2580. https://doi.org/10.1093/bioinformatics/btp426.

74. Yang, J.-S., Nam, H.-J., Seo, M., Han, S.K., Choi, Y., Nam, H.G., Lee, S.-J., and Kim, S. (2011). OASIS: Online Application for the Survival Analysis of Lifespan Assays Performed in Aging Research. PLoS One *6*, e23525. https://doi.org/10.1371/journal.pone.0023525.

75. Stirling, D.R., Swain-Bowden, M.J., Lucas, A.M., Carpenter, A.E., Cimini, B.A., and Goodman, A. (2021). CellProfiler 4: improvements in speed, utility and usability. BMC Bioinformatics *22*, 433. https://doi.org/10.1186/s12859-021-04344-9.

76. Stiernagle, T. (2006). Maintenance of C. elegans. WormBook, 1–11. https://doi.org/10.1895/wormbook.1.101.1.

77. Bibli, S.I., Hu, J., Looso, M., Weigert, A., Ratiu, C., Wittig, J., Drekolia, M.K., Tombor, L., Randriamboavonjy, V., Leisegang, M.S., et al. (2021). Mapping the Endothelial Cell S-Sulfhydrome Highlights the Crucial Role of Integrin Sulfhydration in Vascular Function. Circulation *143*, 935–948. https://doi.org/10.1161/CIRCULATIONAHA.120.051877.

78. Okkenhaug, H., Chauve, L., Masoudzadeh, F., Okkenhaug, L., and Casanueva, O. (2020). Worm-align and Worm_CP, Two Open-Source Pipelines for Straightening and Quantification of Fluorescence Image Data Obtained from Caenorhabditis elegans. J. Vis. Exp. e61136. https://doi.org/10.3791/61136.

79. Byrne, J.J., Soh, M.S., Chandhok, G., Vijayaraghavan, T., Teoh, J.-S., Crawford, S., Cobham, A.E., Yapa, N.M.B., Mirth, C.K., and Neumann, B. (2019). Disruption of mitochondrial dynamics affects behaviour and lifespan in Caenorhabditis elegans. Cell. Mol. Life Sci. *76*, 1967–1985. https://doi.org/10.1007/s00018-019-03024-5.

80. Escorcia, W., Ruter, D.L., Nhan, J., and Curran, S.P. (2018). Quantification of Lipid Abundance and Evaluation of Lipid Distribution in Caenorhabditis elegans by Nile Red and Oil Red O Staining. J. Vis. Exp. *133*, 57352. https://doi.org/10.3791/57352.

81. Kim, D., Paggi, J.M., Park, C., Bennett, C., and Salzberg, S.L. (2019). Graph-based genome alignment and genotyping with HISAT2 and

HISAT-genotype. Nat. Biotechnol. *37*, 907–915. https://doi.org/10.1038/s41587-019-0201-4.

82. Liao, Y., Smyth, G.K., and Shi, W. (2014). featureCounts: an efficient general purpose program for assigning sequence reads to genomic features. Bioinformatics *30*, 923–930. https://doi.org/10.1093/bioinformatics/btt656.
83. Love, M.I., Huber, W., and Anders, S. (2014). Moderated estimation of fold change and dispersion for RNA-seq data with DESeq2. Genome Biol. *15*, 550. https://doi.org/10.1186/s13059-014-0550-8.
84. Chambers, M.C., Maclean, B., Burke, R., Amodei, D., Ruderman, D.L., Neumann, S., Gatto, L., Fischer, B., Pratt, B., Egertson, J., et al. (2012). A cross-platform toolkit for mass spectrometry and proteomics. Nat. Biotechnol. *30*, 918–920. https://doi.org/10.1038/nbt.2377.
85. McCracken, N.A., Peck Justice, S.A., Wijeratne, A.B., and Mosley, A.L. (2021). Inflect: Optimizing Computational Workflows for Thermal Proteome Profiling Data Analysis. J. Proteome Res. *20*, 1874–1888. https://doi.org/10.1021/acs.jproteome.0c00872.
86. Miljkovic, J.L., Burger, N., Gawel, J.M., Mulvey, J.F., Norman, A.A.I., Nishimura, T., Tsujihata, Y., Logan, A., Sauchanka, O., Caldwell, S.T., et al. (2022). Rapid and selective generation of H2S within mitochondria protects against cardiac ischemia-reperfusion injury. Redox Biol. *55*, 102429. https://doi.org/10.1016/j.redox.2022.102429.
87. Doll, S., Freitas, F.P., Shah, R., Aldrovandi, M., da Silva, M.C., Ingold, I., Goya Grocin, A., Xavier da Silva, T.N., Panzilius, E., Scheel, C.H., et al. (2019). FSP1 is a glutathione-independent ferroptosis suppressor. Nature *575*, 693–698. https://doi.org/10.1038/s41586-019-1707-0.
88. Drekolia, M.-K., Talyan, S., Cordellini Emídio, R., Boon, R.A., Guenther, S., Looso, M., Dumbović, G., and Bibli, S.-I. (2022). Unravelling the impact of aging on the human endothelial lncRNA transcriptome. Front. Genet. *13*, 1035380. https://doi.org/10.3389/fgene.2022.1035380.
89. Wider, G., and Dreier, L. (2006). Measuring Protein Concentrations by NMR Spectroscopy. J. Am. Chem. Soc. *128*, 2571–2576. https://doi.org/10.1021/ja055336t.
90. Cullen, C.H., Ray, G.J., and Szabo, C.M. (2013). A comparison of quantitative nuclear magnetic resonance methods: internal, external, and electronic referencing. Magn. Reson. Chem. *51*, 705–713. https://doi.org/10.1002/mrc.4004.
91. Jeanclos, E., Schlötzer, J., Hadamek, K., Yuan-Chen, N., Alwahsh, M., Hollmann, R., Fratz, S., Yesilyurt-Gerhards, D., Frankenbach, T., Engelmann, D., et al. (2022). Glycolytic flux control by drugging phosphoglycolate phosphatase. Nat. Commun. *13*, 6845. https://doi.org/10.1038/s41467-022-34228-2.
92. Ng, D.H.J., Chan, L.Y., Fitzner, L., Keppler, J.K., Ismail, S.M., Hird, S., Hancock, P., Karin, S., and Tobias, D. (2023). A novel screening method for free non-standard amino acids in human plasma samples using AccQ·Tag reagents and LC-MS/MS. Anal. Methods *15*, 445–454. https://doi.org/10.1039/D2AY01588A.
93. Kasarla, S.S., Flocke, V., Saw, N.M.T., Fecke, A., Sickmann, A., Gunzer, M., Flögel, U., and Phapale, P. (2024). In-vivo tracking of deuterium metabolism in mouse organs using LC-MS/MS. J. Chromatogr. A *1717*, 464691. https://doi.org/10.1016/j.chroma.2024.464691.
94. Vlaski-Lafarge, M., Loncaric, D., Perez, L., Labat, V., Debeissat, C., Brunet de la Grange, P., Rossignol, R., Ivanovic, Z., and Bœuf, H. (2019). Bioenergetic Changes Underline Plasticity of Murine Embryonic Stem Cells. Stem Cells *37*, 463–475. https://doi.org/10.1002/stem.2965.
95. Burger, N., Logan, A., Prime, T.A., Mottahedin, A., Caldwell, S.T., Krieg, T., Hartley, R.C., James, A.M., and Murphy, M.P. (2020). A sensitive mass spectrometric assay for mitochondrial CoQ pool redox state in vivo. Free Radic. Biol. Med. *147*, 37–47. https://doi.org/10.1016/j.freeradbiomed.2019.11.028.
96. Lowry, O.H., Rosebrough, N.J., Farr, A.L., and Randall, R.J. (1951). PROTEIN MEASUREMENT WITH THE FOLIN PHENOL REAGENT. J. Biol. Chem. *193*, 265–275. https://doi.org/10.1016/S0021-9258(19)52451-6.
97. Black, M.J., Bertram, J.F., and Johnston, C.I. (2001). Effect of angiotensin-converting enzyme inhibition on myocardial vascularization in the adolescent and adult spontaneously hypertensive rat. J. Hypertens. *19*, 785–794. https://doi.org/10.1097/00004872-200104000-00016.

STAR★METHODS

KEY RESOURCES TABLE

REAGENT or RESOURCE	SOURCE	IDENTIFIER
Antibodies		
anti-4-HNE, rabbit polyclonal	Invitrogen	Cat# BS-6313R; RRID: AB_2827741
anti-SIRT1, rabbit polyclonal	Proteintech	Cat# 13161-1-AP; RRID: AB_10646436
anti-TOM20, rabbit polyclonal	Proteintech	Cat# 11802-1-AP; RRID: AB_2207530
anti-GPD1, rabbit polyclonal	Proteintech	Cat# 13451-1-AP; RRID: AB_10646471
anti-PGC1 alpha, rabbit polyclonal	Novus Biologicals	Cat# NBP1-04676; RRID: AB_1522118
anti-VEGFR2, mouse monoclonal	Santa Cruz Biotechnology	Cat# sc-6251; RRID: AB_628431
anti-GAPDH, mouse monoclonal	Santa Cruz Biotechnology	Cat# sc-47724; RRID: AB_627678
anti-PAX-7, mouse monoclonal	Santa Cruz Biotechnology	Cat# sc-81648; RRID: AB_2159836
WGA-AF488	Invitrogen	Cat# W11261
Anti-Ac-Lysine, mouse monoclonal	Santa Cruz Biotechnology	Cat# sc-32268; RRID: AB_627898
anti- β-tubulin	Sigma Aldrich	Cat# T0198; RRID: AB_477556
anti-CSE	Proteintech	Cat# 12217-1-AP; RRID: AB_2087497
anti-Vinculin	Invitrogen	Cat# MA5-11690; RRID: AB_10976821
anti-S6	Cell Signaling Technology	Cat# 2217; RRID: AB_331355
anti-pS6	Cell Signaling Technology	Cat# 2211; RRID: AB_331679
anti-mouse-AF488, goat polyclonal	Abcam	Cat# ab150113; RRID: AB_2576208
anti-mouse-AF680, goat polyclonal	Abcam	Cat# ab175775
anti-rabbit-AF680, donkey polyclonal	Abcam	Cat# ab175772
anti-rabbit-CY5, goat polyclonal	Invitrogen	Cat# A10523; RRID: AB_2534032
anti-rabbit-HRP	Abcam	Cat# ab205718; RRID: AB_2819160
anti-mouse-HRP	Cell Signaling Technology	Cat# 7076S;RRID: AB_330924
Bacterial and virus strains		
OP50-1	Caenorhabditis Genetics Center	N/A
Chemicals, peptides, and recombinant proteins		
Chelex-100	Sigma Aldrich	Cat# C7901
HEPES	VWR	Cat# 441485H
1M HEPES solution	Sigma Aldrich	Cat# H0887
EDTA	Sigma Aldrich	Cat# E5134
Neocuproine	Sigma Aldrich	Cat# N1501
IGEPAL	Thermofisher	Cat# J61055
SDS	Carl-Roth	Cat# 2326.2
TRIS	Carl-Roth	Cat# 5429.3
Sodium deoxycholate	Sigma Aldrich	Cat# D6750
Glycine	Carl-Roth	Cat# 3187.5
Ponceau S	Sigma Aldrich	Cat# P3504
Tween	Sigma Aldrich	Cat# P9416
Triton X-100	Sigma Aldrich	Cat# T8787
Protease inhibitor cocktail	Sigma Aldrich	Cat# P8340
4-Chloro-7-nitrobenzofurazan (NBF-Cl)	Sigma Aldrich	Cat# 163260
1,4-dithiothreitol (DTT)	ThermoFisher	Cat# R0861
Iodoacetamide	Sigma-Aldrich	Cat# I1149
Ammonium bicarbonate	Sigma Aldrich	Cat# 09830
Calcium chloride	Euromedex	Cat# T885-A
Guanidine hydrochloride	Sigma Aldrich	Cat# G3272

(*Continued on next page*)

Continued

REAGENT or RESOURCE	SOURCE	IDENTIFIER
Triethylammonium bicarbonate buffer	Sigma Aldrich	Cat# 18597
Hydroxylamine solution	Sigma Aldrich	Cat# 467804
Trypsin	Promega	Cat# V5117
TMT10plex	Thermo Scientific	Cat# 90110
DCP-Bio1	Merck	Cat# NS1226
Copper (II)-TBTA complex	Lumiprobe	Cat# 21050
L-ascorbic acid	Sigma-Aldrich	Cat# A92902
Formic acid Suprapur	Supelco	Cat# 111670
TCEP	Sigma-Aldrich	Cat# 646547
AQC	Synchem	Cat# s041
AccQ-Tag Ultra Borate Buffer	Waters	Cat# 186009283
Cyanine5 alkyne	Lumirpobe	Cat# A30B0
Laemmli (4X) buffer	BioRad	Cat# 1610747
β-mercaptoethanol	Sigma Aldrich	Cat# M3148
Western Blotting Luminol Reagent	Santa Cruz Biotechnology	Cat# sc-2048
Ponceau S	Sigma Aldrich	Cat# P3504
Hydrogen Peroxide Solution	Sigma Aldrich	Cat# 216763
Erastin	Sigma Aldrich	Cat# E7781
1S,3R-RSL 3	Sigma Aldrich	Cat# SML2234
Thiazolyl Blue Tetrazolium Bromide	Sigma Aldrich	Cat# M5655
Methyl viologen dichloride hydrate	Sigma Aldrich	Cat# 856177
Sodium (meta)arsenite	Santa Cruz Biotechnology	Cat# sc-250986
Nile Red	Sigma Aldrich	Cat# 72485
Oil Red O	Sigma Aldrich	Cat# O0625
Bovine Serum Albumin	Sigma Aldrich	Cat# A7906
L-(+)-Ergothioneine	Thermo Scientific	Cat# J67861.03
L-Hercynine	Sigma Aldrich	Cat# SMB00978
DMEM	Gibco	Cat# 21969-035
DMEM, high glucose, no glutamine, no methionine, no cystine	Gibco	Cat# 21969-035
DMEM/F-12	Gibco	Cat# 21041025
DMEM, no phenol-red	Gibco	Cat# 31053028
Endothelial Cell Growth Medium 2 (ECGM2)	PromoCell	Cat# C-22011
Fetal bovine serum	Pan Biotech	Cat# P30-3031
L-glutamine	Pan Biotech	Cat# P64-80100
Penicillin-streptomycin	Pan Biotech	Cat# P66-07100
Polybrene	Santa Cruz Biotechnology	Cat# 28728-55-4
Lipofectamine™ RNAiMAX	Invitrogen	Cat# 13778075
DPBS	Sigma Aldrich	Cat# D8537
Hoechst 33342	Sigma Aldrich	Cat# B2261
L-Cystine	Sigma Aldrich	Cat# 30200
Pierce™ High Capacity NeutrAvidin™ Agarose beads	Thermofisher	Cat# 20357
Pierce™ NeutrAvidin™ Agarose beads	Thermofisher	Cat# 29200
DTAB	Thermo Scientific	Cat# A10761.09
Sodium disulfide	Dojindo Molecular Technologies	Cat# SB-02
Dihydroxyacetone phosphate hemimagnesium salt hydrate	Sigma Aldrich	Cat# 51269

(*Continued on next page*)

Continued

REAGENT or RESOURCE	SOURCE	IDENTIFIER
β-Nicotinamide adenine dinucleotide, reduced disodium salt hydrate	Sigma Aldrich	Cat# N8129
Bio-Spin® P-6 Gel Columns	Bio-Rad	Cat# 7326227
Lead(II) acetate trihydrate	Thermo Scientific Acros	Cat# 423841000
Pyridoxal 5'-phosphate hydrate	Thermo Scientific	Cat# A12323
Granulated agar	BD Difco	Cat# BD 214530
Bacto™ Peptone	Gibco	Cat# 211677
LB Broth (Lennox)	Carl Roth	Cat# X964.1
NaCl	Carl-Roth	Cat# HN00.2
Potassium dihydrogen phosphate	Carl-Roth	Cat# P018.2
Di-sodium hydrogen phosphate dihydrate	Carl-Roth	Cat# 4984.1
Potassium phosphate dibasic	Euromedex	Cat# PB0447-B
Agarose D5	Euromedex	Cat# D5-C
Ethanol	Fisher BioReagents	Cat# BP2818500
TRIzol™ Reagent	Invitrogen	Cat# 15596026
Phenol:chloroform:isoamyl alcohol mix (25:24:1)	Sigma Aldrich	Cat# 77617
DMSO	Carl-Roth	Cat# 4720.3
Methanol, Optima™ LC/MS Grade	Fisher Scientific	Cat# A456-212
Trichloromethane/Chloroform	Carl-Roth	Cat# 7331.1
Acetone ROTIPURAN® ≥99.8%	Carl-Roth	Cat# 9372.2
Acetonitrile	Biosolve	Cat# 00012041001BS
Acetic acid	ThermoFisher	Cat# A/0406/PB15
Isopropanol	Fisher Chemicals	P/7507/17
Ammonia solution 28-30%	Sigma Aldrich	Cat# 5.33003
NaOH	Carl-Roth	Cat# 1CCX.2
Hydrochloric acid 1N	Carl-Roth	Cat# K025.1
Trifluoroacetic acid	Biosolve	Cat# 00202341A8BS
Glycerol-3-phosphate dehydrogenase (GDH)	Roche	Cat# 10127752001
GST protein, tag-free	Sigma Aldrich	Cat# SRP5348
Human recombinant CSE, GST-tagged	From Prof. Bibli	Hu et al.[66]
Human recombinant CSE	From Prof. Ruma Banarjee	Wedmann et al.[67]
BODIPY™ 581/591 C11	Invitrogen	Cat# D3861
SF7-AM	Cayman Chemicals	Cat# 14623
Critical commercial assays		
DC protein assay	Biorad	Cat# 5000112
NAD/NADH-Glo™	Promega	Cat# G9081
NADP/NADPH-Glo™	Promega	Cat# G9071
PureLink™ RNA Mini Kit	Invitrogen	Cat# 12183018A
Glycerol-3-Phosphate Assay Kit	Sigma Aldrich	Cat# MAK207
L-Lactate Assay Kit	Sigma Aldrich	Cat# MAK443
Oxaloacetate Assay Kit	Sigma Aldrich	Cat# MAK070
Pyruvate Assay Kit	Sigma Aldrich	Cat# MAK071
Pierce™ High pH Reversed-Phase Peptide Fractionation Kit	Thermo Scientific	Cat# 84868
Deposited data		
Total proteome, persulfidome; Thermal proteome profiling data	PRIDE repository	PXD051587; PXD051609

(*Continued on next page*)

Continued

REAGENT or RESOURCE	SOURCE	IDENTIFIER
RNA Seq data	BioProject database	PRJNA1178314
Raw data for graphs	This paper	Data S1
Experimental models: Cell lines		
Mouse: MEF WT (Male)	From Prof. Snyder's lab (Johns Hopkins University School of Medicine)	Sbodio et al.[68]
Mouse: MEF CSE$^{-/-}$ (Male)	From Prof. Snyder's lab (Johns Hopkins University School of Medicine)	Sbodio et al.[68]
Human: HUVEC		N/A
Human: HEK293T		N/A
Experimental models: Organisms/strains		
C. elegans Wild-Type Bristol N2	Caenorhabditis Genetic Center	N/A
C. elegans: strain MRF03 (*cth-1(ok3319)V*)	Caenorhabditis Genetic Center	strain VC2569
C. elegans: strain MRF09 *mpst-3(tm4387)V*	MITANI Lab, National Bio-Resource; Project of the MEXT, Japan	strain FX04387
C. elegans: strain *CF1038 (daf-16 (mu86)I)*	Caenorhabditis Genetic Center	N/A
C. elegans: strain *SJ4103 (zcIs14 [Pmyo-3::mitoGFP])*	From A.M. Vizuete (The Institute of Biomedicine of Seville)	N/A
C. elegans: strain RB1373 *(F47G4.3(ok1558) I)*	Caenorhabditis Genetic Center	N/A
C. elegans: strain RB1482 *(K11H3.1(ok1733) III)*	Caenorhabditis Genetic Center	N/A
Male Wistar Rat	Institute for Biological Research "Sinisa Stankovic", Belgrade, Serbia	N/A
Oligonucleotides		
siRNA directed against human CSE	Eurogentec	custom synthesis
Recombinant DNA		
psPAX2	Didier Trono Lab	Addgene Plasimd #12260
pMD2.G	Didier Trono Lab	Addgene Plasimd #12259
Cdt-mKO		Riken, Japan
Geminin-GFP		Riken, Japan
Software and algorithms		
R Environment	The R Project for Statistical Computing	https://www.r-project.org/
R studio	RStudio, Inc	https://www.rstudio.com/
PEAKS ONLINE	Bioinformatics Solutions Inc.	http://www.bioinfor.com/
ImageJ	Schneider et al.[69]	https://imagej.nih.gov/ij/download.html
Fiji	Schneider et al.[69]	https://imagej.net/software/fiji/
BioVenn	Hulsen et al.[70]	https://www.biovenn.nl/
GraphPad Prism 10.2.0	GraphPad Software	https://www.graphpad.com
FragPipe	Kong et al.[71]	https://fragpipe.nesvilab.org/
DAVID Bioinformatics Database v6.8	Huang et al.[72]	https://david.ncifcrf.gov/
EigenMS R script	Karpievitch et al.[73]	https://rdrr.io/bioc/ProteoMM/src/R/EigenMS.R
Origin, Version 2022	OriginLab Corporation, Northampton, MA, USA	N/A
ChemDraw 20.0.0.38	PerkinElmer Informatics, Inc	N/A
Adobe Illustrator 28.4.1	Adobe	https://www.adobe.com/products/illustrator.html
BioRender		https://www.biorender.com/
Oasis	Yang et al.[74]	https://sbi.postech.ac.kr/oasis/
CellProfiler	Stirling et al.[75]	
SeamDock	Murail et al.[29]	https://bioserv.rpbs.univ-paris-diderot.fr/services/SeamDock/

EXPERIMENTAL MODELS AND SUBJECT DETAILS

C. elegans

The following strains were used in this study: wild-type (N2), cth-1(ok3319)V, daf-16 (mu86)I, mpst-3(tm4387)V, zcIs14[Pmyo-3::mitoGFP], F47G4.3(ok1558) I, K11H3.1(ok1733) III. Worms were grown at 20 °C on standard nematode growth medium (NGM) seeded with E. coli OP50-1 grown for 16 hours (37 °C with shaking at 180 RPM) as a food source. Worm maintenance was performed following standard techniques.[76] 5-Fluoro-2′-deoxyuridine (FuDR) was not used in this study.

Cell lines

WT and $CSE^{-/-}$ Mouse Embryonic Fibroblasts (MEF) were grown in DMEM (4.5 g/L glucose) supplemented with 2 mM L-glutamine, 1% penicillin-streptomycin and 10% fetal bovine serum at 37°C and 5% CO_2. Human umbilical vein endothelial cells (HUVEC) were isolated and cultured as described[77] and cells up to passage 3 were used for the experiments. The use of human material in this study conforms to the principles outlined in the Declaration of Helsinki and the isolation of endothelial cells was approved in written form by the ethics committee. HEK293T cells were cultured in DMEM/F-12 supplemented with 10% fetal bovine serum, 100 U/mL penicillin-streptomycin and 0.01 mol/L HEPES.

Wistar rats

Nine-month-old male and eight-week-old male and female Wistar rats were housed in the animal facility of the Institute for Biological Research ''Sinisa Stankovic'', National Institute of the Republic of Serbia under the standard dark–light cycle (12 h light–12 h dark) and received commercial food and fresh water ad libitum. All experimental procedures were approved by the Ethics Committee of the Institute for Biological Research ''Sinisa Stankovic'' (App. No. 2-12/12 and No. 000169446 2024 14841 002 001 000 001) according to Directive 2010/63/EU. The animals were divided into two groups: control and ET-treated (20 mg/kg ET in drinking water for either 5 days or 3 weeks).

METHOD DETAILS

Origin of all chemicals are detailed in STAR Methods. Buffers were prepared with Nanopure water and treated with Chelex-100 resins to remove traces of metal ions. All other experimental details are included either in the manuscript text, STAR Methods or in the text that follows.

C. elegans experiments

C. elegans lifespan experiments

For lifespan experiments, worms were synchronized by picking several adults onto NGM plates and allowing them to lay eggs for 3h. Synchronized young adults (D0) were transferred to 35-mm plates containing a final concentration of 0.45 mM ET or vehicle plates containing the same volume of water. Treatment was added on top of the seeded plates, left to dry for a few hours and used on the same day. For the experiments on dead bacteria, seeded plates were exposed to UV light for 10 min followed by the addition of the treatment. The efficacy of the killing protocol was checked by inoculating bacteria from UV-irradiated plates onto a fresh LB plate and incubating for 24 h at 37 °C. Lack of bacterial colonies indicated efficient killing. Worms were grown on live bacteria until D0 and then transferred to treated plates with dead bacteria. Each plate contained ~ 25 animals which were transferred every second day by picking and scored every day. Worms which crawled off the plate, contained bagged worms or vulva protrusion were censored. Death was scored as a failure to move in response to gentle prodding of animals with a platinum wire. Each lifespan experiment was repeated at least twice in a blinded manner.

For the automated lifespan (3 g KH2PO4, 7.5 g Na2HPO4, 5 g NaCl, 1 mL 1 M MgSO4, per L) experiments using Nemalife lifespan machine, worms were grown on regular NGM plates without treatment until D0. Young adults were washed with M9 and approximately 70 animals were loaded per microfluidic chip using syringe and blunt-end needle. Every day the chips were washed for 90 s with liquid NGM to remove progeny followed by 90 s recording of animals' survival and movement. Worms were then fed with 20 mg/mL OP50 in light NGM supplemented with the treatment or vehicle solution. Briefly, 30 μL of ET or Herc stock solutions in H_2O were mixed with 970 μL of concentrated OP50 to reach final concentrations of 5 mM treatment and 0.01% DMSO. Chips were stored in the incubator at 20 °C. Survival counts were determined using the Nemalife analysis suite (Nemalife Inc., TX). Briefly, 90-second recorded videos were segmented into three still-image frames (30s, 60s, 90s), with a bounding box automated around each animal. Animals were deemed alive if more than half their body length had displaced outside of the bounding box between two still-image intervals (i.e., > half body length displacement in the 90s vs 60s frame). Animals unable to move from the encompassing box across all three frames were deemed dead. All videos were manually corrected for any falsely implemented annotations made by the analysis software.

C. elegans thrashing rates

On the day of analysis, individual animals were picked into 10 μL of M9 buffer on Superforst microscope slides (to avoid cuticle adhesion to slides) and were allowed to adapt to liquid environments for approximately 10 s. Thrashing rates were then counted for 20 s, with each full bend of the head and tail to one side marked as a count. Overall rates are displayed as thrashing counts per minute based on 20 s count. All experiments were performed in at least two biological replicates.

C. elegans stress-assays

Worms were grown on treatment or vehicle plates from D0 of adulthood until the desired age for stress-assay tests. For paraquat stress assays, 1 mL of 250 mM paraquat solution in H_2O was added on top of seeded plates containing 3 mL of NGM (final concentration 62.5 mM) and were allowed to dry at room temperature (RT) for 4 hours. Worms were subsequently transferred to vehicle / paraquat plates, with survival monitored every hour until >80% of the population had died. For heat shock exposure, worms were transferred to fresh plates and incubated at 35 °C. Survival was scored every hour. For arsenite and H_2O_2 stress-assays, animals were picked into individual wells of a 96-well plate in 50 μL of M9 buffer. Freshly prepared stocks of sodium (meta) arsenite and H_2O_2 were dissolved in M9 buffer and prepared such that 50 μL of the solution was added to each well to a final volume of 100 μL at the indicated toxicant concentration (H_2O_2: 100 μM, arsenite: 5 mM at D4 and 2 mM at D10). Animals were assessed as being dead or alive by the presence or absence of a movement response to gentle tapping of the plates every hour. All experiments were performed in at least two biological replicates by two different researchers.

C. elegance autofluorescence measurement

For live imaging, worms were picked by hand and placed in a drop of M9 buffer on a 2 % agarose pad. Imaging was performed using a Leica SP8 LIGHTNING Confocal Microscope and HC PL FLUOTAR 10X/0.30 air objective. The following excitation/emission settings were used: blue (405/460±25 nm), green (488/525±25nm), red (514/640±30 nm), in accordance with previous work.[18] Acquired Z-stack images were load into ImageJ and compiled together with the Sum slices function. These images were then loaded into the Worm-align Bioformat in Fiji[78] to straighten all animals and perform fluorometric intensity analysis of the three respective autofluorescence wavelengths. Brightness and contrast parameters were kept the same for all images within each fluorescent wavelength assessed. Worm-align was used to curate masks of each individual animal, and these metadata were uploaded into CellProfiler for quantification of fluorescence intensity of whole animals.

C. elegans mitochondrial imaging

SJ4103 animals were grown on vehicle or ET plates until D10. Worms were then picked by hand in a drop of M9 without any anaesthetic compounds (given their potent mitochondria-inhibiting properties) and carefully immobilized via cover slips. Recording was performed with an HC PL IRAPO 40 x/1.10 water objective and excitation/emission settings 488/520 ± 20 nm were used. Images of body-wall muscle cells were taken from both head and tail regions of each animal, avoiding vulval midbodies that exhibit frequent egg-laying induced tissue disruption. For morphological quantification, images were analyzed in Fiji using the Mosaic Suite SQUASSH (segmentation and quantification of subcellular shapes; http://mosaic.mpi-cbg.de/) as previously described[79] Image segmentation, to optimise computational annotations of mitochondrial networks and remove background interference, was performed in line with others[79]: a background removal window size of 15 pixels, regularization of 0.07 and a minimum GFP fluorescence-intensity of 0.2. The SQUASSH plugin was then used to calculate individual mitochondrial size and perimeter, allowing the two-dimensional calculation of mitochondrial circularity: [circularity = $(4 \times \pi) \times (\text{Area}/\text{Perimeter}^2)$], fitting objects to a perfect circle and measuring its deviation from this where 1 = a perfect circle and 0 = a straight line. Data were then analyzed and presented as Gaussian distribution plots of mitochondrial circularity scores, using bins of 0.05 μm.

C. elegans Nile Red staining

D10 adults were collected and washed three times with PBST (PBS + 0.01% Tween). Worms were then fixed in 40% isopropanol for 3 min at RT while gently mixing. Traces of fixation solution were removed by two PBST washes and animals were immediately incubated in Nile Red staining solution following the protocol.[80] Briefly, working solutions were prepared by adding 6 μl of Nile Red stock solution (0.05% in acetone) in 1 mL of 40% isopropanol. After 2 h of staining at RT in the dark, the solution was removed and worms were washed in PBST and mounted on glass slides. Images were recorded on a Leica SP8 LIGHTNING Confocal Microscope using an HC PL FLUOTAR 10X/0.30 air objective and excitation/emission wavelengths 488/588±27 nm.

C. elegans Oil Red staining

D10 adults were collected, washed two times with M9 and fixed in MRWB solution for 1 h at RT with occasional mixing. Worms were shortly centrifuged, supernatant was removed and pellet was washed 2 times with PBS + 0.1 % Triton X-100. Dehydration was performed by incubating worms in 60% isopropanol for 15 min. Worms were collected, supernatant removed and 600 μl of Oil Red working solution was added and incubated at 37 °C to stain the lipids. After 4 h, the dye was removed, and its excess was washed out 2 times for 30 min with PBS + 0.1 % Triton X-100. Worms were mounted on glass slides and recorded on a Leica DM6 B light microscope using HC PL FLUOTAR 10x/0.32 dry objective. Oil Red stock solution was prepared by dissolving 0.5 *g* of Oil Red O in 100 ml of isopropanol, while working solution was prepared by diluting the stock solution with H_2O to reach 60% isopropanol. The working solution was then left to mix overnight at RT and it was filtered before the use.

C. elegans RNA sequencing

For RNA extraction, worms were synchronized by bleaching, and maintained as described above, with a few modifications. Worms were transferred every day using M9 buffer. Animals were collected from plates and washed at least three times with M9 using gravity to remove bacteria and progeny. After the last wash, worms were spread over the treatment or vehicle plates. On the day of collection, 80 animals were transferred into a 1.5 ml tube, washed three times with M9 and excess buffer was removed. 500 μL of Trizol reagent was immediately added to the worm pellet and samples were flash frozen in liquid nitrogen. Samples were subjected to three freeze-thaw cycles (fast thawing in the water bath followed by 30 s vortexing and direct freezing in liquid nitrogen). After the third cycle, 200 μL of phenol/chloroform/ isoamyl alcohol mix (25/24/1, v/v/v) was added, samples were vigorously shaken by hand for 15 s, incubated for 2 min at RT and centrifuged at 12,000 x g for 15 min. The upper aqueous phase was carefully transferred to a new tube and mixed with an equal volume of 70% ethanol in RNase free water. RNA purification was further performed using

PureLink ® RNA Mini Kit following manufacturer's protocol. RNA quality and yield were checked using a NanoDrop spectrophotometer and immediately frozen at -80 °C. Sequencing was performed by the Beijing Genomic Institute (BGI, Hong Kong) using DNBSEQ™ sequencing technology. High-quality adapter-free reads were directly mapped to the C. elegans reference genome (WBCel235) using HISAT2 v. 2.1.0. [81] Following duplicate removal, gene-level read assignments were performed with featureCounts v. 1.6.4.[82,83] Differential gene expression analysis was conducted using DESeq2 v. 1.42.1.

C. elegans persulfidome

For persulfidome analysis, worms were synchronized by bleaching. Isolated eggs were placed in M9 buffer and incubated for 14 h at 20 °C with gentle shaking (130 rpm) to hatch. In order to have enough starting material and avoid starvation, worms were grown on 100-mm NGM plates (~ 1000 worms/plate) and transferred every day using M9 buffer. Plates were prepared by adding 1 mL of treatment or vehicle stock solution (10 mM aqueous ET solution) on top of the seeded plates (20 mL of NGM and 1 mL of *E. coli* OP50-1). The plates were left to dry overnight under the hood and used the day after. On the day of collection worms were collected into 15-mL falcons and washed at least three times to remove bacteria and progeny. After the last wash, M9 was removed and pellet corresponding to 150 μL was flash frozen in liquid N_2 and used for downstream analysis. Worm pellets were kept on ice and quickly defrosted by addition of 1 mL HEN lysis buffer (50 mM HEPES, 1 mM EDTA, 0.1 mM Neocuproine, 1% IGEPAL, 2% SDS, pH 7.4) supplemented with 10 mM NBF-Cl and 1% protease inhibitor prior to use. Suspension was mixed well and transferred to 15 mL Bioruptor® Pico Tubes (Diagenode, C30010017) containing 200 μL of glass beads. Samples were lysed by sonication in Biorputor Pico at +4 °C. Lysates were incubated for 2 h at 37 °C followed by centrifugation at 18,000 x *g* for 15 min at 4 °C to remove debris. Proteins were precipitated twice by methanol/chloroform precipitation (water/methanol/chloroform, 4:4:1, v/v/v) and washed twice with ice-cold methanol. Pellets were dissolved in PBS supplemented with 0.2% SDS and equal amounts of protein were incubated with Pierce™ NeutrAvidin™ Agarose beads to remove endogenously biotinylated proteins. After 2 h of mixing at room temperature, supernatant was removed and precipitated once. Proteins were suspended in PBS supplemented with 2 % SDS and incubated for 1.5 h at 37 °C with 250 μM DCP-Bio1 to specifically label persulfides. Excess probe was removed by precipitation and obtained pellets were dissolved in PBS supplemented with 0.1% SDS and adjusted to equal protein amount. Samples were then incubated for 4 h at RT with Pierce™ High-Capacity Streptavidin Agarose to enrich persulfidated proteins. Unbound proteins and detergent were removed by washing the beads with 28 mL of PBS and 8 mL of H_2O on Pierce™ disposable columns. Enriched proteins were eluted by incubating the beads with 2.25 M ammonium hydroxide solution for 16 h at RT. Eluates were then collected from the columns, lyophilized and subsequently dissolved in digestion buffer (50 mM ammonium bicarbonate (ABC), 1 mM $CaCl_2$). Trypsin was added at enzyme/protein ratio 1/20 and digestion was performed at 37 °C for 16 h. Samples were desalted using Oasis HLB cartridges (Waters, WAT094225). Peptides were dissolved in 0.1 % TFA, and quality control was performed using an Ultimate 3000 Nano Ultra High-Pressure Chromatography (UPLC) system with a PepSwift Monolithic® Trap 200 μm * 5 mm (Thermo Fisher Scientific).

Sample were analyzed by high-resolution LC-MS/MS using an Ultimate 3000 Nano Ultra High-Pressure Chromatography (UPLC) system (Thermo Fisher Scientific) coupled with an Orbitrap Eclipse™ Tribrid™ Mass Spectrometer via an EASY-spray (Thermo Fisher Scientific). Peptide separation was carried out with an Acclaim™ PepMap™ 100 C18 column (Thermo Fisher Scientific) using a 180 min gradient: 0 min, 3% B; 115 min, 28% B; 125 min, 35% B (solvent B corresponds to 84% acetonitrile, 0.1% formic acid) at a flow rate of 250 nL/min. The Orbitrap Eclipse™ was operated in a DDA mode and MS1 survey scans were acquired from m/z 300 to 1,500 at a resolution of 120,000 using the Orbitrap mode. The most intense ions were isolated for 3 s with a 1.2 m/z window and then fragmented by high-energy collision-induced dissociation (HCD) with a normalized collision energy of 32%, considering a dynamic exclusion of 30 s. MS/MS spectra were recorded using normal speed IonTrap mode.

For full proteome analysis used to normalize persulfidome data, 150 μg of original NBF-Cl samples were diluted with PBS and precipitated to remove traces of SDS. Protein pellets were resuspended in 6 M guanidine hydrochloride (GuHCl) and 40 μg of protein was taken from each sample for further steps. Samples were diluted with digestion buffer to reach final concentration of 0.3 M GuHCl. All other steps were performed in the same way as abovementioned. Samples were analyzed using a 180 min gradient: 0 min, 3% B; 120 min, 30% B; 125 min, 35% B at a flow rate of 250 nL/min. All other parameters were the same as for persulfidome data except dynamic exclusion which was set at 40 s.

Data were evaluated in PEAKS ONLINE software using 15 ppm precursor mass error tolerance, 0.5 Da fragment mass error tolerance, specific trypsin digestion and maximum 3 missed cleavages. For persulfidation detection, NBF (+163.00961594 Da) on C, K, R, DCP (+168.0786442 Da) on C, N-term acetylation (+42.010565 Da), and methionine oxidation (+15.994915 Da) were added as variable modifications. For total proteome detection NBF (+163.00961594 Da) on C, K, R, N-term acetylation (+42.010565 Da), and methionine oxidation (+15.994915 Da) were added as variable modification. PSM and proteins were filtered at FDR 1 %. Data was normalized in R studio using EigenMS. [73] Total proteome data were normalized based on the total ion count (TIC).

C. elegans proteomics

D4 and D10 animals were collected (~ 200 worms/condition) as previously described. Worm pellets were defrosted by adding 40 μL of 7.5 M GuHCl in 50 mM ABC. Samples were boiled for 5 min at 95 °C, left to cool down and then sonicated in Biorputor Pico at +4 °C in the presence of glass extraction beads. Debris was removed by centrifugation at 20,000 x *g* for 10 min at 4 °C. Protein content was determined and 40 μg of protein was taken for further processing. Samples were reduced with 5 mM DTT for 1 h at 37 °C, shaking at 300 rpm and then alkylated for 30 min in the presence of 20 mM idoacetamide. Digestion and desalting steps were performed as previously described. After quality control, peptides were analyzed by high-resolution LC-MS/MS using an Ultimate 3000 Nano Ultra High-Pressure Chromatography (UPLC) system (Thermo Fisher Scientific) coupled to a timsTOF Pro (Bruker) equipped with a CaptiveSpray source. Peptide separation was carried out with an Acclaim™ PepMap™ 100 C18 column (Thermo Fisher Scientific)

using a 95 min linear gradient from 3 to 38 % of B (84% Acetonitrile, 0.1% Formic Acid) at a flow rate of 400 nL/min. The timsTOF Pro2 (Bruker) was operated in PASEF mode using Compass Hystar 5.0.36.0. The TIMS setting was as follows: Mass Range 100 to 1700 m/z, 1/K0 Start 1.6 Vs/cm^2 End 1.6 Vs/cm^2, Ramp time 100 ms, Lock Duty Cycle to 100%, Capillary Voltage 1500 V, Dry Gas 3 L/min, Dry Temp 180°C. PASEF settings: 10 MS/MS scans, charge range 0-5, active exclusion for 0.4 min, Scheduling Target intensity 20000, Intensity threshold 2500, CID collision energy 49 eV. Data were evaluated with PEAKS ONLINE software using 15 ppm for precursor mass tolerance, 0.5 Da for fragment mass tolerance, specific trypsin digestion, and a maximum of 2 missed cleavages. Carbamidomethylation (+57.021464 Da) on C, N-term acetylation (+42.010565 Da), and methionine oxidation (+15.994915 Da) were added as variable modifications, PSM and proteins were filtered at FDR 1 %. Data was normalized based on the total ion count (TIC).

MALDI imaging of C. elegans

Ergothioneine standard (10 mM) was mixed 1:2 (v/v) ratio with CHCA matrix (10 mg/ml in 70:30 CH_3OH/H_2O + 0.2% TFA) and spotted onto a stainless-steel plate for MALDI analysis by dried droplet method. MALDI analysis was then carried out using the parameters stated below, with confirmatory MS/MS also performed on standards at normalised collision energy 15, with isolation mass m/z 230. D4 N2 and *cth-1* worms were collected in M9 and washed 5 times with 1 mL of H_2O to clean animals from bacteria and remove salts from buffer solution. Worms were pipetted onto glass slides in 20 μL of H_2O and immediately dried under vacuum to remove residual water from the slide before matrix spraying. CHCA matrix (5 mg/mL in 80% Methanol + 0.2% TFA) was applied to the sample using a Sunchrom SunCollect pneumatic sprayer. Matrix was applied in 10 layers using 1st layer at 10 μL/min, 2nd layer at 20 μL/min and 3rd layer plus at 30μL/min at a speed of 'Low 10' (775 mm/s) for the x-axis and 'Medium 1' (850 mm/s) for the y-axis. Gas pressure was set to 2.8 bar and z-height at 10 mm. MSI experiments were performed on an Orbitrap QExactive HF mass spectrometer (Thermo Fisher Scientific GmbH, Bremen, Germany) coupled to an elevated pressure MALDI ion source (Spectroglyph LLC, Kennewick, WA, USA). The 349-nm MALDI laser was operated at a repetition rate of 500 Hz and pulse energy of ~2 μJ. The laser was focused to a spot size of 20 μm and the pixel sizes for analyses were 25x25μm for the worms. The high-pressure funnel (HPF) and low-pressure funnel (LPF) were operated at 98 Vpp and 75 Vpp, respectively, using 720 kHz and 825 kHz respectively. The high-pressure funnel region was held at 7 Torr for analysis. The mass spectrometer was operated in positive mode with AGC mode turned off. Resolution was set at 120,000 for m/z 200 with a mass range of m/z 50 to 600 and a set inject time of 250 ms was used, resulting in 125 shots/pixel. Instrument calibration was performed with ESI and using Thermo Pierce Calmix. Complimentary microscopy images were captured using brightfield Keyence VHX-7000N. Serial stitched images were performed using the 200x magnification.

Preliminary images were viewed in ImageInsight (Spectroglyph) and MSI processing was further performed in LipostarMSI (Molecular Horizons). Thermo RAW (.raw) and positional files (.xml) were converted to imzML files using the built-in converter for LipostarMSI, which utilises msconvert from ProteoWizard (3.0.22317) for initial conversion to mzML format. The imzML file was then loaded into LipostarMSI using the following parameters: 5 ppm m/z tolerance, peak intensity >1%, peak detection frequency >1% and minimum spatial chaos >0.7. Hotspot removal was applied using the 99% quantile and no denoising was applied.

Detection of 4-HNE protein adducts in aged C. elegans

Worm NBF-Cl lysates were used for detection of 4-hydroxinonenal protein adducts (4-HNE). Equal protein amounts were loaded onto 10% polyacrylamide gels, resolved by SDS-PAGE and transferred to a nitrocellulose membrane. After 1 h of blocking in 5% BSA in TBST (TBS + 0.1% Tween), membranes were incubated with anti-4-HNE antibody (1:1000 in 1% BSA in TBST) overnight at +4 °C. Membranes were then washed five times with TBST and incubated for 1.5 h with secondary anti-rabbit AF680 antibody (1:20 000, 1% BSA in TBST). Levels of 4-HNE (IR short filter, 680 nm) and total protein amount (Cy2 filter, 488 nm) were visualized using Amersham Typhoon imager (Cytiva), with 4-HNE intensities normalized to total protein load.

NAD^+ measurement in C. elegans

50 animals were hand-picked into a 1.5 ml tube and washed 3 times with M9. After the last wash, worms were kept in 30 μl of M9, immediately frozen in liquid nitrogen and stored at -80 °C until all samples were collected. Once defrosted, mixtures of 60 μl 0.2 M NaOH + 1 % dodecyltrimethylammonium bromide (DTAB) and 30 μl of M9 was added to each sample (final sample volume was 120 μl). 20 μl of glass beads was quickly added to the tubes and the samples were sonicated in Bioruptor at +4 °C (5 cycles, 1 cycle: 30 s on, 30 s off). Lysates were then centrifuged at 15 000 x g for 10 min at +4 °C, and the supernatant was used for quantification of NAD^+ using the NAD/NADH-Glo™ assay kit, following the manufacturer's protocol. Samples were incubated with the kits Glo-reporter for 60 min at RT, and luminescence was recorded on a CLARIOstar Plus plate reader (BMG LABTECH; Ultra-Glo, 540-50nm).

Cell experiments

Temperature range thermal proteome profiling (TPP)

MEF cells were grown until 90% confluency and then incubated with 400 μM ET (or vehicle control) for 4 h. TPP was performed using the previously described method.[27] Briefly, cells were trypsinized and centrifuged at 300 x g for 3 min. Cell pellets were washed twice with PBS at RT and resuspended in 600 μl of PBS. 100-μL aliquots were added into 0.2-mL PCR tubes and cells were then exposed to 10 different temperatures (25, 37.4, 40.4, 43, 45.7, 48.7, 52.5, 55.5, 58.2, 60.9, 63.8 °C) for 5 min. Samples were cooled down in a water bath at 25 °C for 5 min and then lysed in 100 μl of PBS with 0.1% NP40 by three freeze-thaw cycles. Lysates were ultracentrifuged for 20 min at 100 000 x g, and the supernatant was collected. Reduction and alkylation were carried out by first incubating the samples with 1 mM DTT for 1 h at 37 °C followed by 30 min incubation at 37 °C with 5 mM iodoacetamide. Samples were diluted to 0.3 M GuHCl using ABC buffer and digested with a 1:20 trypsin ratio. Desalted peptides were resuspended in 100 mM triethylammonium bicarbonate (TEAB) and labeled using TMT10plex™ Isobaric Label Reagents following the manufacturer's protocol. After

quenching the reaction with 0.4% of hydroxylamine, samples were desalted and dried. Remaining traces of detergent were removed on Detergent Removal Spin columns (Thermo Scientific, Cat# 87777) and peptide quality control was carried out as previously described. Samples were fractionated using Pierce™ High pH Reversed-Phase Peptide Fractionation Kit (Thermo Scientific, Cat# 84868) to increase protein identification and coverage.

Fractions were analyzed by high-resolution LC-MS/MS using a Dionex UltiMate 3000 RSLC Systems (RSLC) system (Thermo Fisher Scientific) coupled with an Orbitrap Eclipse™ Tribrid™ Mass Spectrometer via an EASY-spray (Thermo Fisher Scientific). Peptide separation was performed with an Acclaim™ PepMap™ 100 C18 column (Thermo Fisher Scientific) using a 120 min non-linear gradient (Fraction 1: 0 min, 3% B; 120 min, 35 % B; F2, F3, F4, F5: 0 min, 3 % B; 5 min, 9 % B; 120 min, 35 % B; F6, F7: 0 min, 3 % B; 5 min, 11 % B; 120 min, 35 % B; F8: 0 min, 3 % B; 8 min, 15 % B; 120 min, 35 % B) at a flow rate of 250 nL/min. The Orbitrap Eclipse™ was operated in a DDA mode, and MS1 survey scans were acquired from m/z 300 to 1,500 at a resolution of 120,000 using the Orbitrap mode. MS2 scans were carried out for 3 seconds with high-energy collision-induced dissociation (HCD) at 32 % using the Orbitrap mode at a resolution of 50,000. Thermo ".Raw" files were converted into mzML files using proteowizard tool.[84] The search was performed using FragPipe's [71] pre-built TMT 10 workflow. Briefly, 20 ppm was used for the precursor and the fragment mass tolerance. Enzymatic cleavage was set for trypsin and 2 missed cleavages. TMT precursor mass (+ 229.16293 Da) on K and peptide N-terminus as well as carbamidomethylation (+ 57.02146 Da) on C residue were used as fixed modifications. Oxidation (+15.9949 Da) on M residue and N-terminal acetylation (+42.0106 Da) were set as variable modifications. PSM and proteins were filtered using FDR 1 %. No normalization was applied in Fragpipe. Data analysis was then performed using the computational workflow InflectSSP[85] on Rstudio providing normalization of protein abundancies, curve fitting function, p-value and FDR adjusted p-value for comparison between ET and vehicle-exposed cells.

Isothermal dose-response (ITDR) profiling of CSE

WT MEFs were grown until 85-90% confluency before collection. ITDR was performed following previously described protocol.[27] Briefly, cells were trypsinized and washed as previously described in TPP protocol. Cells were lysed in PBS supplemented with 0.1% NP40 and lysate was centrifuged at 20 000 x g for 20 min to remove debris. Supernatant was adjusted to 1mg/ml and split into 9 tubes. Lysates were then incubated with different concentration of ET (1000, 800, 700, 600, 400, 300, 200, 100 and 0 μM) for 30 min at 25° followed by incubation at 53°C for 5 min. Samples were then incubated at 25°C for 5 min to cool down and ultracentrifuged at 100,000 x g for 20 min. Supernatant was collected and flash frozen for further processing. Control sample (0 μM) was used to normalize protein amount to 30 μg between biological replicates. Protein reduction, alkylation, tryptic digestion, TMT labelling and peptide fractionation were performed as described in TPP section. The fractions were analyzed by high resolution LC-MS as previously described with the following modifications: 60 min non-linear gradient (Fraction 1-7: 0 min, 3% B; 60 min, 35 % B; F8: 0 min, 3 % B; 20 min, 20 % B; 60 min, 35 % B) at a flow rate of 250 nL/min. The search against mouse CSE fasta file was performed in FragPipe using the previously described TMT workflow. Raw abundances were normalized to 126 channel (1000 μM ET). Data representation and non-linear curve fit were performed in GraphPad Prism.

Intracellular H_2S imaging

WT and $CSE^{-/-}$ MEF cells were plated in an 8-well chambered coverslip (IBIDI) at 20 000 cells per well, stained with fluorescent sensor SF7-AM as described previously[86] and treated according to the experimental set up. Following treatment, cells were incubated with 1 μM Hoechst in DMEM for 20 min and the media was then replaced with phenol red-free DMEM. All images were acquired using 20 ms exposure, 5% laser intensity and excitation/emission 488/525 nm for SF7-AM and 200 ms exposure, 20% laser intensity and excitation/emission 405/450 nm for Hoechst. Images were acquired using a Zyla 4.2 PLUS sCMOS camera attached to an Andor DragonFly 500 confocal spinning disk mounted on a Nikon Eclipse TiE microscope using a CFI Plan Apochormat lambda 100X oil immersion objective. Images were analyzed using Fiji ImageJ. The image processing workflow was automated using the following novel Fiji ImageJ macro scripts written by Dr Roy Chowdury in Dr Julien Prudent's laboratory (MRC Mitochondrial Biology Unit, University of Cambridge, Cambridge, UK). The integrated density of 10–50 cells per replicate was used to quantify fluorescence intensity.

MEF cell proliferation

MEF cells were seeded at a density of 2,500 cells/well in a 96-well plate in full medium and left overnight to attach. The next day, in order to remove traces of cysteine, wells were washed twice with non-cysteine containing media. Cells were then incubated with media supplemented with 10% FCS, standard concentration of methionine and different concentration of L-cystine (0 – 200 μM) and ET (0 – 400 μM) for 20 h. Media was removed and MTT reagent, diluted in media, was added to the wells and incubated for 3 h. Crystals formed on the cell surfaces were dissolved in isopropanol supplemented with 4 mM HCl and 0.1% NP40. Absorbance was measured at 562 nm using Multiscan FC Microplate Photometer (Thermo Scientific).

Cell survival assays

10,000-20,000 cells were seeded per well in 96-well plate and treated according to the experimental design. Following defined treatment, cells were exposed to MTT reagent as described.

Measurement of lipid peroxidation using C11-BODIPY (581/591)

MEF WT cells were treated with different concentrations of ET for 24 h and then exposed to 1 μM RSL3 for 3 h. Further steps were performed as previously described.[87] Sample acquisition was performed on a Cytek Biosciences Aurora 5L spectral flow cytometer. Median fluorescence intensity of the raw data channel B2-A (525/17 nm) was extracted and further analyzed.

HUVEC cell cycle monitoring

HEK293T cells were plated in a density of 40,000 cells/cm^2 and 24 h later were co-transfected with psPAX2, (Addgene plasmid #12260), pMD2.G (Addgene plasmid #12259) and the target plasmids (Cdt-mKO and Geminin-GFP, Riken) in the presence of polyethylamine (1 μg/μL, Sigma). Supernatant containing viral particles were collected 72 and 96 h after transfection, filtered through a 0.45 μm filter and stored in -80 °C until use. HUVECs were transduced for 24 hours with 1:1 ECGM-2: Viral volumes in the presence of 8 μg/ml polybrene (Santa Cruz). After transduction, cells were seeded in 96 well plates at a density of 4,000 cells per well and monitored under a live cell imaging system (Incucyte S3, Sartorius)

HUVEC proliferation

HUVEC were seeded onto 24 well plates (Sarstedt, Germany) at a density of 15,000 cells/well. Cells were treated with control siRNA (50 pmol) or siRNA directed against CSE (50 pmol, custome synthesis, Eurogentec) using Lipofectamine RNAiMAX (Invitrogen, Karlsruhe, Germany) for 72 h prior to experimentation. 16 images/well at magnification × 10 were taken every 4 h using an IncuCyte S3 live-cell analysis system (Essen BioScience, United Kingdom). Cell confluence was measured for up to 4 days. Image processing and analysis were performed using the following parameters: segmentation adjustment 1.8; clean up: hole fill 0 μm2; adjust size (pixels): 0; filter: minimum 350 μm2 area, no maximum, eccentricity: no minimum, no maximum.

Sprouting

The spheroid sprouting assay was performed as previously described.[88] At least five spheroids per group were analyzed for each cell batch.

NAD$^+$ measurement in cells

MEF WT cells were grown in 96-well plates and treated with different concentrations of ET for 18 h. Treatment was removed and ice-cold 1:1 mixture of PBS and 0.2 M NaOH + 1 % DTAB (135 μl) was added to each well. Plate was shaken in orbital shaker at 300 rpm for 3 min to enable homogeneous cell lysis.

^{1}H NMR detection of ET in cell extracts

MEF WT and CSE$^{-/-}$ cells were grown in 100-mm dishes and treated for 16 h with 200 μM ET. On the next day (90% confluent cells), treatment was removed, and cells were washed twice with ice-cold PBS. The dish was quickly placed into a liquid nitrogen bath and incubated for 2 min. The plate was then moved to ice, 1.5 ml of ice-cold absolute methanol was added, and cells were thoroughly scraped and collected into 15 ml Bioruptor® Pico tubes. Lysates were sonicated in Bioruptor Pico at +4 °C (5 cycles, 1 cycle: 30 s on, 30 s off) followed by centrifugation at 18,000 x *g* for 10 min. The supernatant was carefully removed and evaporated dry in a SpeedVac, retaining and utilizing protein pellets for normalization of sample amounts. Shortly, the pellets were dissolved in 50 mM HEPES supplemented with 2% SDS and protein concentration was determined using DC protein assay.

Samples were prepared for NMR analysis by dissolving the samples in 600 μL D_2O. Additionally a 1 mM solution of 3-(Trimethylsilyl) propionic-2,2,3,3-d$_4$ acid (TMSP-d$_4$) was added as internal standard and transferred to a 5 mm borosilicate NMR tube. The software TopSpin 3.6.5. was used for the signal acquisition and processing of the NMR spectra. All measurements were performed at 7 °C. For signal acquisition, a double watergate pulse sequence with excitation sculpting for water suppression was used to acquire the 1H NMR spectra. A relaxation delay of 5 s was selected. The radio frequency power of 62.5 kHz was used to perform the μ and μ/2 pulses which were combined with 2 ms selective rectangular shape pulses to efficiently suppress the 1H resonance of the H_2O. The latter was chosen as the transmitter frequency (O1). Signal accumulation was achieved by 512 scans for each spectrum with an acquisition time of 1.7 s. The data were processed by using Fourier transformation, zero and first order phase correction, automatic baseline correction and by applying a 0.3 Hz line broadening using a Lorentzian window function. For an absolute concentration determination ERETIC2 reference was used.[89,90] To calibrate an ERETIC reference a 10 mmol/L sucrose solution was used as a calibration compound. Based on the sucrose refence, an electronic signal was placed in each NMR spectrum and the signal corresponding to the calibration compound was integrated and normalized according to the number of protons of this compound.[91]

Metabolic analysis of metabolites from transsulfuration pathway

MEF WT cells were grown in 60-mm dishes and treated or not with 400 μM ET for 2h in full medium. Cells were washed two times with warm PBS and collected by trypsinization. Trypsin was quenched, cells were centrifuged for 5 min at 300 x g, washed two more times with PBS and cell pellets were frozen in liquid nitrogen. Metabolites were extracted by addition of 350 μL of ice-cold methanol supplemented with 0.1 % formic acid and 5 mM TCEP. The cell lysate was sonicated in Bioruptor Pico at +4 °C and vortexed to improve metabolite extraction. Samples were then centrifuged at 15000 rpm for 30 min at 4 °C, supernatants were collected and dried in SpeedVac. The protein concentrations were measured from the pellets using BCA assay and used for post-acquisition data normalization. Dried extracts were dissolved in 80 μL of borate buffer and 20 μL of AQC reagent was added to derivatize amino acids. Samples were incubated for 1 min at RT followed by incubation at 55 °C for 10 min. The reaction mixtures were cooled on ice and transferred to clean autosampler inserts for LC-MS/MS analysis.

LC-MS/MS analysis of derivatized amino acids

Amino acid-AQC derivatives were identified and quantified using liquid chromatography (Vanquish Duo UHPLC; Thermo Fisher Scientific, Waltham, MA, USA) coupled with Orbitrap Fusion Lumos Tribrid Mass Spectrometer (Thermo Fisher Scientific, Waltham, MA, USA). Briefly, 3 μL of the final reaction mixture was injected and separated using a reversed-phase AccQ·Tag Ultra C18 (1.7 μm, 2.1 × 100 mm; Waters Corporation, Milford, USA) column with a flow rate of 0.4 mL/min. The binary solvent system consists of mobile phase A (water) and mobile phase B (ACN) both buffered with 0.1% formic acid. The elution gradient conditions were as follows: 0.1 % B, 0–0.54min; 9.1 % B, 5.74 min; 21.2 % B, 7.74 min; 90 % B, 10 min; 90 % B, 12 min; 0.1% B, 12.5–18 min.[92] The MS datasets were acquired in positive-ion mode within the mass range of 65–850 m/z. The optimized heated electrospray ionization (HESI) source

and data-dependent acquisition parameters were used as described earlier.[93] Precursor ion m/z, retention time, and fragmentation pattern of the amino acid-AQC derivatives were established and verified using authentic metabolite standards of cysteine (292.0751 m/z, 5.16 min) and homocysteine (306.0907 m/z, 6.13 min). Whereas, accurate mass ($\leq$ 3 ppm) and diagnostic fragment ion (171.0547 m/z) were used to confirm the cystathionine-AQC derivative (563.1707 m/z, 5.94 min). In cell extracts, amino acid-AQC derivatives were identified and quantified according to the precursor ion m/z, retention time, and diagnostic fragment ions. Chromatogram and mass spectral data were processed to obtain peak area values using the Quan Browser application in Xcalibur software (Thermo Fisher Scientific). The final quantitative results were normalized to the protein concentrations and relative changes across the samples were expressed as arbitrary units.

Persulfidation detection in cell lysates

MEF WT cells were grown in T75 flask and lyzed under native conditions at 90% confluency. After two washes with cold PBS, 1 ml of RIPA buffer (50 mM Tris, 150 mM $NaCl_2$, 2 mM EDTA, 1 % IGEPAL, 0.5 % sodium deoxycholate, 0.1 % SDS, pH 7.4) was added. Cells were gently scraped, lysate was collected and additionally homogenized with syringe and needle. Insoluble parts were removed by centrifugation at 20,000 x g for 10 min at +4 °C and protein concentration was measured. Lysates were then split into 3 tubes: CON (without ET and SDS), ET (with ET without SDS) and ET+SDS (with both ET and SDS). 20% SDS solution was added to the ET+SDS tube to reach 2%, and the same volume of H_2O was added to the other two tubes. ET (final concentration 400 μM) or H_2O were then added to corresponding tubes. After 30 min incubation at RT, SDS was quickly added to non-SDS-containing tubes to denature the proteins and lysates were blocked with 5 mM NBF-Cl for 1 h at 37 °C. Samples were precipitated by methanol/chloroform precipitation and the pellets were washed as described. Proteins were suspended in HEPES + 2 % SDS, adjusted and switched to selectively label persulfides using Dimedone Switch method.[26] The same protein amounts were mixed with Laemmli 4X buffer supplemented with 10% β-mercaptoethanol. Samples were boiled for 5 min at 95 °C and resolved by SDS-PAGE. Gels were recorded on Amersham Typhoon at 635 nm for Cy5, and 488 nm for NBF-Cl signal which was used as a loading control.

Bioenergetic analysis by XF24e Analyzer

Oxygen consumption rate (OCR), as an indicator of cellular respiration, and extracellular acidification rate (ECAR), as an indicator of lactate and bicarbonate production, were determined simultaneously using an XF2e Analyzer.[94] WT or $CSE^{-/-}$ MEFs were plated at a density of 7.5 × 10^4 cells per well in a 24-well XF V7 plate (BD Bioscience), incubated overnight in the presence or absence of ET, washed, resuspended in appropriate assay medium and analyzed. OCR and ECAR were reported as an average of three differential absolute rates (pmoles/min for OCR and mpH/min for ECAR). All experiments were repeated at least three times. Modulators used for Seahorse measurements were provided by Sigma-Aldrich, MO, USA. Parameters of the mitochondrial respiration were evaluated in the assay medium consisting of bicarbonate-free DMEM (SeaHorse Bioscience) supplemented with 25 mM glucose, 1 mM pyruvate, and 2 mM glutamine. Mitochondrial respiration was monitored in the basal state and after sequential injections of the mitochondrial modulators oligomycin (1 μM), 2,4-dinitrophenylhydrazine (DNP, 100 μM), and antimycin (ANT)/rotenone (ROT); 1 μM both). Glycolytic activity is estimated in the assay medium and the base medium without any exogenous fuel substrate supplementation. ECAR values were estimated in the basal state and after sequential injections of 10 mM glucose, oligomycin (1 mM), 2-deoxyglucose (2-DG; 100 mM).

Intracellular CoQ redox state

The CoQ redox state was determined by mass-spectrometry as described previously.[95] WT and $CSE^{-/-}$ MEF cells (1 x 10^6 cells / plate) were washed rapidly with cold PBS twice and then scraped into 200 μL PBS, added to a mixture of 300 μL acidified methanol (0.1% (w/v) HCl) and 250 μL hexane and vortexed to extract CoQ. The hexane phase was separated by centrifugation at 17,000 × *g* for 5 min. The hexane (top) layer was transferred into MS vials and dried under the stream of nitrogen. The crude residue from samples was resuspended in 200 μL methanol containing 2 mM ammonium formate, overlaid with Argon and analysed by LC-MS/MS using an I-Class Acquity LC system attached to a Xevo TQ-S triple quadrupole mass spectrometer (Waters). Samples were stored in a refrigerated autosampler (8 °C) and 2 μL sample was injected into a 15 μL flowthrough needle and separated by RP-HPLC at 45 °C using an Acquity C18 column (2.1 × 50 mm, 1.7 μM; Waters). The isocratic mobile phase was 2 mM ammonium formate in methanol used at 0.8 mL/min over 5 min. The mass spectrometer was operated in positive ion mode with multiple reaction monitoring. The following settings were used for electrospray ionisation in positive ion mode: capillary voltage – 1.7 kV; cone voltage – 30 V; ion source temperature –100 °C; collision energy – 22 V. Nitrogen and argon were used as curtain and collision gases, respectively. Transitions used for quantification were: UQ9, 812.9 > 197.2; UQ9H2, 814.9 > 197.2. Samples were quantified using MassLynx 4.1 software to determine the peak area for UQ9 and UQ9H2

Biochemical experiments

Two different sources of human recombinant CSE were used in this study[66,67] (Data S1).

Measurement of CSE-catalyzed H_2S production from ET

The experiment was performed following previously described procedures with small modifications.[30] Briefly, 100 mM HEPES (pH 7.4), 0.4 mM lead acetate, 9 μg of CSE, or 3 μg of CSE-GST and different combinations of substrates were mixed in a final volume of 1 mL. Reactions were recorded on an Agilent Cary 8454 UV-VIS Spectrophotometer (Agilent Technologies) for 5 min at 37 °C, where an increase of absorbance at 390 nm directly corresponded to H_2S production and lead sulfide formation. H_2S concentration was calculated using molar extinction coefficient for lead sulfide determined for this experimental design (8178 M^{-1} cm^{-1}).

Michaelis-Menten kinetics of human recombinant CSE with ET

The kinetics of H_2S release was continuously monitored by formation of lead sulfide as described above. Since we observed that the solution of 0.4 mM lead acetate in 100 mM HEPES (pH 7.4) is not stable unless cysteine is present (milky white opalescence is formed within minute), which prevented us from directly measuring the reaction of ET and CSE, we opted for establishing those kinetic parameters indirectly using competitive two-substrate equation and the equimolar mixture of ET and cysteine. Knowing the actual concentration of ET and cysteine and by separately establishing the K_m and V_{max} for cysteine as a substrate, we could estimate the Michaelis-Menten kinetic parameters for the reaction of ET with CSE.

Measurement of ET desulfuration in presence of CSE

Purified CSE (10 μg/mL) in 100 mM HEPES (pH 7.4) was mixed with 1 mM ET and the reaction mixture was incubated at 37 °C. Every minute, an aliquot was taken and immediately combined with 1 mM NBF-Cl solution and 2% SDS in the same buffer. After 30 min at 37 °C, the solution was transferred to a 1-cm cuvette and recorded on UV-Vis spectrophotometer. ET concentration for each time point was calculated based on the standard curve including different ET concentrations.

LC-MS detection of CSE-catalyzed hercynine formation

100 μM ET was mixed with 1.5 μg of CSE and incubated in 50 mM HEPES for 10 min at RT. Every minute, aliquot was taken and mixed with ACN (1:1, v/v). LC/MS analysis was performed on I-Class ACQUITY UPLC system (Waters) coupled with Waters Xevo TQ-S Mass Spectrometer. The binary solvent system consisted of solvent A (5% ACN, 0.1% formic acid) and solvent B (90% ACN, 0.1% formic acid). Samples were separated on I-Class ACQUITY UPLC BEH C18 column (1 x 50 mm, 130 Å, 1.7 μm, Waters) using the following gradient: 0-1 min, 5% B; 3-4 min, 50% B; 6-8 min, 100% B; 8-15 min, 5% B. The MS datasets were required in positive ion mode.

NMR spectroscopy of PLP and ET reaction

1H NMR measurements were performed on a Bruker Avance III HD spectrometer operating at 400 MHz. The 1H NMR spectra of pure PLP and ET in D2O were used to identify the product in the studied sample. It is worth mentioning, that -NH aromatic protons of ET were not observable under those conditions. In order to monitor reaction over time, 1H NMR spectrum of equimolar PLP-ET mixture was recorded every 1 h at 298 K.

UV-Vis spectra of PLP and ET reaction

100 mM HEPES (pH 7.4), 1.5 mM ET and 150 μM PLP were mixed in a final volume of 1 mL and the reaction was conducted at RT. UV-Vis spectra were recorded every minute for total of 3 h and the product formation was monitored at 333 nm.

ESI-TOF MS monitoring of PLP or CSE reaction with ET

Mass spectrometry was performed on maXis 5G, Bruker Daltonic (Bremen, Germany), an ESI-TOF MS capable of resolution of at least 40,000 FWHM.

Measurement of GPDH activity

Glycerol-3-phosphate dehydrogenase (GPDH) from rabbit muscle was diluted in 50 mM HEPES (pH 7.4) to reach a final concentration of 13.3 nM (0.5 ng / μL) and added into black 96-well plate. Sodium disulfide (Na_2S_2) was dissolved in ultrapure H_2O just before use and quickly added in 1:0, 1:0.1, 1:1 and 1:5 enzyme to Na_2S_2 ratio. Dihydroxyacetone phosphate (DHP) was then added to a final concentration of 0.4 mM and a reaction volume of 100 μL. Detection was performed in a CLARIOstar Plus plate reader (BMG LABTECH) and recorded for 5 min at 37 °C before NADH (0.2 mM final) was injected by the machine to initiate the reaction. A decrease in fluorescence corresponding to consumption of NADH was monitored using a monochromator with excitation/emission wavelengths of 355 ± 20/455 ± 30 nm, respectively.

Detection of GPDH persulfidation by MS

GPDH from rabbit muscle was cleaned on Bio-Spin® P-6 Gel columns to remove traces of original storage solution. Concentrated protein was further diluted with 50 mM TRIS pH 7.4 to reach a concentration of 1.15 mg/mL. 15 μg of protein was used for each condition (final concentration in reaction was 26.6 μM). The same volume of different Na_2S_2 stock solutions (freshly dissolved in ultrapure H_2O) was added to reach different protein to Na_2S_2 ratios (1:0, 1:1, 1:2, 1:5, 1:10). The mixture was incubated for 15 min at 37 °C and immediately quenched with iodoacetamide (100 times excess compared to the highest concentration of Na_2S_2). Proteins were then desaturated by the addition of 7 M GuHCl in 50 mM ABC to reach a final concentration of 3 M. Samples were incubated for 30 min in the dark and then diluted 6 times with 50 mM ABC supplemented with 1 mM $CaCl_2$. Trypsin was added at a 1:20 ratio (0.75 μg) and incubated for 16 h at 37 °C. Samples were further processed for LC/MS measurement as described. Sample were analyzed by high-resolution LC-MS/MS using an Ultimate 3000 Nano Ultra High-Pressure Chromatography (UPLC) system (Thermo Fisher Scientific) coupled with an Orbitrap Q Exactive HF Mass Spectrometer via an EASY-spray (Thermo Fisher Scientific). Peptide separation was carried out with an Acclaim™ PepMap™ 100 C18 column (Thermo Fisher Scientific) using a 150 min gradient: 0 min, 3% B; 95 min, 35% (solvent B corresponds to 84 % acetonitrile, 0.1% formic acid) at a flow rate of 250 nL/min. The Orbitrap Q Exactive was operated in a DDA mode and MS1 survey scans were acquired from m/z 300 to 1,500 at a resolution of 60,000 using the Orbitrap mode. The top 15 most intense ions were isolated with a 1.6 m/z window and then fragmented by HCD with a normalized collision energy of 32%, considering a dynamic exclusion of 12 s. Search against the sequence of rabbit cGPDH was performed in PEAKS ONLINE using described parameters and following variable modifications: carbamidomethylation (+ 57.02146 Da) on C residue, S-carbamidomethylation on C (89.086464), oxidation (+15.9949 Da) on M residue and N-terminal acetylation (+42.0106 Da).

Experiments with rats

Endurance test using treadmill apparatus

Treadmill apparatus for small experimental animals (NeuroSciLaBG-Treadmill, Elunit, Belgrade, Serbia) used in this study comprised of a single moving belt and four plexiglass-separated running compartments. To encourage rats to engage in running, each running compartment featured an electrified metal grid with a low-intensity electric shock (0.2 mA) positioned at the starting edge as negative stimulation, alongside a dark area at the ending edge serving as positive stimulation. Rats were positioned on the moving belt and directed to run in the opposite direction to the belt movement, toward the positive stimulation, while avoiding the negative stimulation. Moreover, using accompanying software, a predetermined protocol for belt movement (duration and speed), as well as belt inclination, was established beforehand. Throughout the entirety of the treadmill protocol, the belt remained at a 0° incline. Prior to endurance tests, rats underwent a period of adaptation and familiarization with the treadmill apparatus over three consecutive days (20 minutes per day, belt speed: 10 m/min). For endurance testing, the initial belt speed was set at 5 m/min for 5 minutes. Subsequently, the speed was incrementally increased by 1 m/min every minute until reaching 21 m/min, where it remained constant. The rats underwent treadmill running until they exhibited signs of exhaustion. Exhaustion was characterized by the rat remaining seated on the metal grid shocker plate for more than 10 seconds without showing any signs of attempting to resume running. The recorded test parameters for each rat were the time to exhaustion in minutes, as well as the total distance covered during the run in meters.

Blood and tissue collection

Animals were euthanized by decapitation. Blood and quadriceps muscle samples were collected and routinely processed for biochemical, microscopic and immunoassays. The relative mass of gastrocnemius muscles was calculated as ratio of muscle/total body weight (mg/mg body weight).

Biochemical serum analysis

After blood isolation, serum was prepared and stored at −80°C until further analysis. Lactate in serum was determined fluorometrically (Shimadzu UV-160 spectrophotometer, Kyoto, Japan) using L-Lactate Assay kit.

Metabolite detection in rat muscle

Detection of different metabolites in rat muscle tissue was performed using commercially available kits. Sample homogenization and metabolite detection was done following the manufacturer's protocol for each metabolite of interest. Oxaloacetate, pyruvate, Gro3P and lactate levels were determined using corresponding kits from Sigma Aldrich. $NADP^+$, NADPH, and NAD^+, NADH abundances were measured using NADP/NADPH-Glo™ and NAD^+/NADH-Glo™ kits from Promega.

Immunoblotting

Homogenates of skeletal rat muscle were prepared in sucrose buffer containing protease and phosphatase inhibitors. Protein content in the samples was estimated by the method of Lowry et al.[96] 10 or 20 μg of total protein extracts were separated by SDS-PAGE and transferred onto polyvinylidene fluoride (PVDF) membranes (10600023, GE Healthcare Life Sciences). After 1 h of blocking in 5% BSA, membranes were incubated overnight with primary antibody followed by incubation with an appropriate secondary antibody. Antigen detection was performed by an enhanced chemiluminescence detection system using an iBright CL1500 Imaging System (Thermo Fisher Scientific). The following primary antibodies were used in this study: anti-vinculin, anti-CSE (1:500), anti-GAPDH, anti-phospho S6, anti-S6, anti-TOM20 (1:1000), anti-VEGFR (1:1000), anti-SIRT1 (1:1000), anti-PGC-1α (1:1000) and β-tubulin (1:2000). HRP-conjugated secondary antibodies were used at following ratios: anti-rabbit (1:20000) and anti-mouse (1:2000). Lysine acetylation levels in rat NBF-Cl samples were detected using anti-Ac-Lysine antibody (1:500) and corresponding secondary antibody. NBF-Cl signal was used as a measure of total protein content.

Microscopy of muscle tissue sections

Immediately after isolation, quadricep muscle tissue was fixed overnight in 10% formaldehyde at 4°C. After 24 h, the tissue was routinely processed for embedding in paraffin blocks. The tissue was cut into 5-μm-thin sections that were deparaffinized with xylene and rehydrated in graded ethanol prior to staining. Antigen retrieval (pH 6.6, microwave boiling, 5 min) and blocking of nonspecific binding with normal goat serum (1:10) were performed before incubation with primary antibodies. Samples were then incubated overnight at 4 °C with mouse anti-wheat germ agglutinin (WGA) (1:100) for assessment of skeletal muscle capillarization. Fluorescently labelled WGA-AF488 is widely used for quantitative assessment of capillarisation by measuring the number of capillary profiles relative to the number of myocyte profiles, capillary density, capillary length and surface area.[97] For the assessment of the MuSCs, the section were stained with anti-Pax-7 antibody (1:200). In the case of Pax-7 detection, the sections were further incubated with secondary goat anti-mouse IgG Alexa Fluor 488 (1:200) antibody, for one hour at room temperature. The nuclei were counterstained with Hoechst 33342 dye (1 μg/mL) and embedded in Mowiol (Sigma-Aldrich). The slides from four animals per group were examined by fluorescent microscopy (Zeiss Imager Z1, AXIO, Carl 4 Oxidative Medicine and Cellular Longevity Zeiss Meditec AG, Germany). Quantification of PAX7-positive stem cells per 100 nuclei is presented. 2–3 images per animal were analyzed.

Electron microscopy

Muscles samples were removed from two animals per group after decapitation and immediately cut into slices. Tissue slices were immersed in 4% glutaraldehyde solution in 0.1 M phosphate buffer (PB) (pH 7.4) for 24 h, and postfixed with 1% OsO4 in the same buffer for 1 h. Samples were dehydrated in a graded ethanol series and embedded in Araldite and Harderner resin. Precise ultrathin sectioning was performed using Leica UC7 Ultramicrotome with a Diatome ultra 45° diamond knife (Diatome, Switzerland). Grids with ultrathin sections were stained with uranyl acetate and lead citrate, and examined under a JEM-1400 transmission electron microscope (TEM, Japan Electron Optics Laboratory Co., Ltd).

Persulfidation levels of cytosolic GPDH in rat muscle tissue

NBF-Cl muscle extracts from vehicle and ET-treated rats were adjusted to equal protein amounts and incubated with 250 μM DCP-Bio1 for 1.5 h at 37 °C. Samples were precipitated and protein pellets were dissolved in PBS supplemented with 1% SDS and adjusted. 30 μg of each sample was taken for estimation of total protein levels, and the rest was diluted up to 0.1% SDS and incubated with 40 μl (slurry volume) of precleaned Pierce™ High-Capacity Streptavidin Agarose for 4 h at RT on ferris wheel. Samples were then centrifuged for 1 min at 500 x g and left to settle for 5 min on ice. Sample supernatants were removed, and beads were washed 2 times with 1 ml of PBS supplemented with 0.01% Tween and 3 times with PBS. Bound proteins were eluted by boiling the beads in 1x Laemmli buffer for 10 min at 95 °C while shaking at 650 rpm. The supernatant was carefully transferred to a new tube and ran on SDS-PAGE. Samples for total GPDH were reduced, boiled and further processed in the same way as persulfidated fractions. After protein transfer and BSA blocking, membranes were incubated with an anti-GPDH antibody (1:1000, 1 % BSA in TBST) and corresponding secondary antibody. Signals were visualized using Amersham Typhoon and ratios of GPDH-SSH to total GPDH was used for comparison.

Activity of cytosolic GPDH in rat muscle tissue

Frozen muscle tissues from vehicle and ET-treated rats were lysed and cGPDH activity estimated following previously described protocol.[53]

QUANTIFICATION AND STATISTICAL ANALYSIS

Plotting of the data was performed using GraphPad Prism version 10.2.0. Western blot, microscopy and gel images were analyzed in Image J. Semantic space, PC analysis and KEGG enrichment bar plots were generated in R studio. Lifespan curves were assessed by Log-rank (Mantel-Cox) in GraphPad. Statistical tests and significances are mentioned in the figure legends. *p<0.05, **p<0.01, ***p<0.001, ****p<0.0001. Illustrations were created by Biorender.com.